Inorganic Chemistry

Article

pubs.acs.org/IC

Chiral Crystallization of a Heterodinuclear Ni-Ln Series: Comprehensive Analysis of the Magnetic Properties.

Fanica Cimpoesu,[†] Françoise Dahan,[‡] Sonia Ladeira,[‡] Marilena Ferbinteanu,*[,§] and Jean-Pierre Costes*[,‡]

[†]Institute of Physical Chemistry, Splaiul Independentei 202, Bucharest 060021, Romania

[‡]CNRS; LCC (Laboratoire de Chimie de Coordination), 205, route de Narbonne, F-31077 Toulouse Cedex 4, France

[§]Inorganic Chemistry Department, Faculty of Chemistry, University of Bucharest, Dumbrava Rosie 23, Bucharest 020462, Romania

Supporting Information

ABSTRACT: Four heterodinuclear $(H_2O)_2$NiL-Ln$(NO_3)_3$ complexes (Ln = Tb, Dy, Er, Yb) with a double phenoxo bridge coming from the dideprotonated Schiff-base ligand are synthesized and characterized by crystal and powder X-ray diffraction studies. This series of compounds devoid of any chiral center, crystallizes in a noncentrosymmetric space group $P2_1$, as the previously described $(H_2O)_2$NiL-Gd$(NO_3)_3$ equivalent. All four complexes are ferromagnetically coupled. If this behavior is clearly shown by the $\chi_M T$ increase at low temperature in the case of the Ni−Tb and Ni−Dy complexes, it necessitates the preparation of the Zn−Er and Zn−Yb equivalent entities to be evidenced in the case of the Ni−Er and Ni−Yb complexes. Out-of-phase susceptibility signals are found in the four cases, but the SMM behavior is neither confirmed, nor completely studied because of the presence of fast quantum tunnelling at zero field. Thorough ab initio multiconfiguration calculations are carried out, achieving a realistic account of ligand field effects, exchange coupling and magnetic anisotropy in the discussed systems. The calculations reveal the ferromagnetic intercenter exchange coupling, the interplay with spin−orbit effects leading to a Ising-like scheme of the lowest levels. The ab initio simulation of the magnetic susceptibility is in semiquantitative agreement with experimental data, certifying the reasonableness of the theoretical treatments in obtaining valuable information for the interacting mechanisms. The anisotropy is accounted for by drawing polar diagrams of state-specific magnetization functions, obtained by handling of the data resulting from ab initio calculations including the spin−orbit effects. Supplementary, Density Functional Theory (DFT) calculations are carried out, presenting new methodological clues and assessments. The DFT is not perfectly adequate for lanthanide systems because of orbital pseudodegeneracy issues. However, we show that in particular circumstances the DFT can be partly used, succeeding here in mimicking different orbital configurations of the Ni−Tb system. The DFT seems to offer reasonable estimations of exchange coupling parameters, while it remains problematic in the complete account of Ligand Field splitting. The Paper presents unprecedented methodological advances and correlations with phenomenological and heuristic interpretation of experimental data, taking into focus relevant d-f systems constructed with a prototypical binucleating ligand.

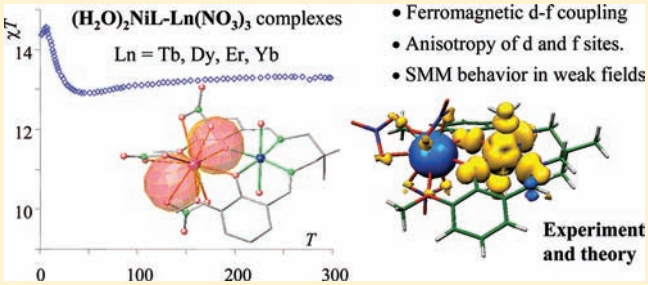

1. INTRODUCTION

In a previous work, we have shown that the compartmental Schiff base *N*,*N*′-2,2′-dimethylpropylenedi(3-methoxydalicylideneiminnato) ligand (L^{2-}) was able to yield a heterodinuclear $(H_2O)_2$NiL-Gd$(NO_3)_3$ complex with a double phenoxo bridge and a ferromagnetic Ni−Gd interaction.[1] This complex, which possesses no chiral center, crystallizes in a noncentrosymmetric space group $P2_1$. This property is not original for it has been demonstrated by a Cambridge Structural Database survey of the 1998 edition that 8% of organic and organometallic achiral compounds generate chirality by crystallization.[2] Such a generation of chirality requires rotation of bonds, helical arrangement, or formation of a head-to-head stacking columnar arrangement. As the most interesting magnetic properties of heterodinuclear 3d-4f complexes come from the series involving the heavy lanthanide ions, we have checked if the isostructurality of the Ni-Ln series is preserved on going from Gadolinium to Ytterbium with help of four examples, Ni−Tb, Ni−Dy, Ni−Er, and Ni−Yb compounds. The magnetic properties of the last two entities have been studied by comparison with the behavior of the Zn-Ln derivatives. The alternating current (ac) susceptibility measurements under applied static field and in the absence of an applied magnetic field have also been undertaken to verify if these Ni-Ln complexes could behave as Single-Molecule Magnets (SMM), a property of large interest for nowadays molecular magnetism.[3,4]

The experimental work is accompanied by theoretical complements, aiming to understand the intricate interplay of exchange coupling, ligand field (LF), and spin−orbit (SO) effects in the molecular magnetism of this prototypical series of molecules. The quantum chemistry of the lanthanides is not

Received: January 24, 2012
Published: March 21, 2012

   dx.doi.org/10.1021/ic3001784 | Inorg. Chem. 2012, 51, 11279−11293

simple, but we succeeded in making it tractable at a level quite transparent to the chemical intuition. The technical problem was identified in the non-*aufbau* nature of the lanthanide ions and the methodological clue was found in initiating the calculations with orbitals assembled from preliminarily prepared fragment orbitals. Thus, the lanthanide ion is treated first separately from the d complex and the outer ligands of the f sphere, the orbitals of the fragments being then merged and submitted to multiconfiguration procedures. This particular methodology[5] was first used for a complex with a binucleating ligand from the same family,[6] the study being dedicated to the celebrated question of the quasi-generalized ferromagnetism in Cu−Gd complexes.[7] Later on, the issue of SMM effect in dinuclears was addressed by the account of a Fe−Dy system.[8] Since the lanthanide ions and magnetism, in general, imply multiconfiguration approaches (to deal with orbital and spin multiplets), the best computational frame belongs to the so-called CASSCF (Complete Active Space Self Consistent Field) methods,[9,10] the above-mentioned particular methodology[5] with merged molecular fragments being accomplished by CASSCF procedures. Interesting breakthroughs in detailed account of anisotropy of the embedded lanthanide ions by the ab initio identification of magnetization axes of ground and excited terms are also developed in this work. The magnetic susceptibility curves (χT vs T) due to lanthanide ion were simulated at the ab initio level, retrieving the experimental trends.

In spite of being popular among chemists, the DFT methods[11] are not easily applicable to the d-f complexes. The non-*aufbau* nature of these systems draws most of the standard computational approaches into severe convergence problems. However, recently, DFT treatments acknowledging also the particular difficulties related with the lanthanide treatment, were reported.[12,13] Using the actual Ni−Tb system as a case study, we proposed an interesting methodological innovation, emulating the elements of the split ^{7}F term of the Tb(III) site from seven self-consistent DFT calculations that permuted the β electron of the f^8 configuration. In summary, interesting experimental and modeling advances, which mutually corroborate each other, are presented. These open new perspectives in the understanding of molecular magnetism of d-f complexes.

2. EXPERIMENTAL AND COMPUTATION DETAILS

2.1. Materials. [LNi]·1.75H_2O,[14] (L: *N*,*N*′-2,2-dimethylpropylenedi(3-methoxy-salicylideneiminato) ligand), and LZn(H_2O)[3] were prepared as previously described. The metal salts Tb(NO_3)$_3$·6H_2O, Dy(NO_3)$_3$·6H_2O, Ho(NO_3)$_3$·6H_2O, Yb(NO_3)$_3$·6H_2O were used as purchased. High-grade acetone (Normapur, VWR) was used for preparing the complexes.

2.2. Syntheses. These complexes were prepared according to the same experimental process, so that only the nickel−terbium entity will be described in detail.

[(H_2O)$_2$NiL-Tb(NO_3)$_3$] ***1***. Addition of Tb(NO_3)$_3$·6H_2O (0.25 g, 0.55 mmol) to a stirred suspension of [LNi]·1.75H_2O (0.2 g, 0.5 mmol) in acetone (10 mL) induced dissolution of the nickel complex with color change. The mixture was stirred at room temperature until reduction of the solvent volume and precipitation of a light purple solid that was isolated by filtration and dried. Yield: 0.25 g (55%). Anal. Calcd for $C_{21}H_{28}N_5NiO_{15}Tb$ (808.1): C, 31.2; H, 3.5; N, 8.7. Found: C, 30.8; H, 3.5; N, 8.2. IR: 3506 m, 3432 m, 2949w, 1644 m, 1629 m, 1607 m, 1510 m, 1473s, 1461s, 1435s, 1408 m, 1391 m, 1327 m, 1292s, 1219s, 1168w, 1067 m, 1030 m, 968w, 928w, 851w, 814w, 744 m, 736 m, 643w, 618w cm^{-1}.

[(H_2O)$_2$NiL-Dy(NO_3)$_3$] ***2***. Yield: 0.21 g (48%). Anal. Calcd for $C_{21}H_{28}DyN_5NiO_{15}$ (811.7): C, 31.1; H, 3.5; N, 8.6. Found: C, 30.8; H, 3.4; N, 8.1. IR: 3508 m, 3434 m, 2949w, 1644 m, 1629 m, 1607 m, 1511 m, 1462s, 1435s, 1408 m, 1391 m, 1327 m, 1293s, 1219s, 1169w, 1068 m, 1030 m, 968w, 928w, 852w, 814w, 744 m, 736 m, 644w, 618w cm^{-1}.

[(H_2O)$_2$NiL-Er(NO_3)$_3$] ***3***. Yield: 0.11 g (30%). Anal. Calcd for $C_{21}H_{28}ErN_5NiO_{15}$ (816.4): C, 30.9; H, 3.5; N, 8.6. Found: C, 30.5; H, 3.4; N, 8.0. IR: 3501 m, 3440 m, 2950w, 1644 m, 1629 m, 1608 m, 1510 m, 1463s, 1435s, 1407 m, 1391 m, 1327 m, 1292s, 1219s, 1169w, 1067 m, 1030 m, 969w, 928w, 852w, 813w, 745 m, 736 m, 644w, 620w cm^{-1}.

[(H_2O)$_2$NiL-Yb(NO_3)$_3$] ***4***. Yield: 0.10 g (27%). Anal. Calcd for $C_{21}H_{28}N_5NiO_{15}Yb$ (822.2): C, 30.7; H, 3.4; N, 8.5. Found: C, 30.3; H, 3.3; N, 8.0. IR: 3504 m, 3440 m, 2979w, 1644 m, 1628 m, 1608 m, 1463s, 1435s, 1407 m, 1391 m, 1327 m, 1292s, 1219s, 1168w, 1068 m, 1030 m, 969w, 928w, 852w, 813w, 745 m, 739 m, 645w, 621w cm^{-1}.

[(H_2O)ZnL-Ho(NO_3)$_3$]·C_3H_6O ***5***. Yield: 0.12 g (30%). Anal. Calcd for $C_{24}H_{32}HoN_5O_{15}Zn$ (860.9): C, 33.5; H, 3.8; N, 8.1. Found: C, 33.3; H, 3.6; N, 7.7. IR: 3572 m, 2961w, 1699w, 1622s, 1464s, 1435s, 1414 m, 1393w, 1318 m, 1289s, 1221s, 1172w, 1061 m, 1031w, 969w, 927w, 851w, 815w, 737 m, 642w, 608w cm^{-1}.

[(H_2O)ZnL-Er(NO_3)$_3$]·C_3H_6O ***6***. Yield: 0.10 g (25%). Anal. Calcd for $C_{24}H_{32}ErN_5O_{15}Zn$ (863.2): C, 33.4; H, 3.7; N, 8.1. Found: C, 33.1; H, 3.5; N, 7.6. IR: 3525w, 3415w, 2952w, 1695w, 1623s, 1466s, 1436s, 1409 m, 1393w, 1320 m, 1290s, 1223s, 1169w, 1064 m, 1031w, 973w, 927w, 851w, 815w, 738 m, 643w, 608w cm^{-1}.

[(H_2O)ZnL-Yb(NO_3)$_3$]·C_3H_6O ***7***. Yield: 0.08 g (20%). Anal. Calcd for $C_{24}H_{32}N_5O_{15}YbZn$ (869.0): C, 33.2; H, 3.7; N, 8.1. Found: C, 32.9; H, 3.5; N, 7.5. IR: 3346w, 3245w, 2959w, 1703w, 1621s, 1467s, 1435s, 1405 m, 1390w, 1288s, 1221s, 1170w, 1063 m, 1034w, 968w, 925w, 851w, 813w, 740 m, 644w, 611w cm^{-1}.

2.3. Physical Measurements. Elemental analyses were carried out at the Laboratoire de Chimie de Coordination Microanalytical Laboratory in Toulouse, France, for C, H, and N. IR spectra were recorded on a Spectrum 100 FT-IR Perkin-Elmer spectrophotometer using the ATR mode. Magnetic data were obtained with a Quantum Design MPMS SQUID susceptometer. Magnetic susceptibility measurements were performed in the 2−300 K temperature range in a 0.1 T applied magnetic field, and diamagnetic corrections were applied by using Pascal's constants.[15] Isothermal magnetization measurements were performed up to 5 T at 2 K. The ac susceptibility measurements were carried out in a 3 G ac field oscillating at 10−1000 Hz, under a 0.1 T static field.

2.4. Crystallographic Data Collection and Structure Determination for (4) and (5). Crystals of **4** and **5** were kept in the mother liquor until they were dipped into oil. The selected crystals of **4** (colorless, 0.50 × 0.35 × 0.25 mm^3) and **5** (pale-yellow, 0.45 × 0.20 × 0.10 mm^3) were mounted on a Stoe Imaging Plate Diffractometer System (IPDS) using a graphite monochromator (λ = 0.71073 Å) and equipped with an Oxford Cryosystems cooler device. The data were collected at 180 K. The unit cell determinations and data integration were carried out using the Xred package.[16] The structures were solved using SHELXS-97 program[17] and refined on F^2 by full-matrix least-squares using SHELXL-97 included in the software package WinGX version 1.63.[18] Atomic scattering factors were taken from the International Tables for X-ray Crystallography.[19] The hydrogen atoms were included in calculated positions and refined as riding atoms using SHELX default parameters. All non-hydrogen atoms were refined anisotropically. The figures were drawn with Zortep.[20]

Crystal Data for ***4***. $C_{21}H_{28}N_5NiO_{15}Yb$, M = 822.23, monoclinic, $P2_1$ (No.4), Z = 2, a = 10.0202(11), b = 15.9443(14), c = 8.8542(10) Å, β = 90.942(13)°, V = 1414.4(3) Å^3, 14028 collected reflections, 5524 unique reflections (R_{int} = 0.0311), R = 0.0205, R_w = 0.0483 for 5436 contributing reflections [$I > 2\sigma(I)$].

Crystal Data for ***5***. $C_{24}H_{32}HoN_5O_{15}Zn$, M = 860.85, triclinic, $P\bar{1}$ (No.2), Z = 2, a = 9.4311(8), b = 9.6841(10), c = 18.3666(17) Å, α = 78.101(11), β = 89.681(11), γ = 75.234(11)° V = 1585.2(3) Å^3, 15894 collected reflections, 5831 unique reflections (R_{int} =0.0323), R = 0.0310, R_w = 0.0542 for 4979 contributing reflections [$I > 2\sigma(I)$].

2.5. Ab Initio Calculations. The calculations were performed with the GAMESS program[21] using the SBKJC[22] effective core potentials

dx.doi.org/10.1021/ic3001784 | *Inorg. Chem.* 2012, 51, 11279−11293

and basis sets for lanthanides, 6-311G* basis set for the Ni, N, or O atoms, and 6-31G for the C or H atoms. The molecular structure is taken for the experimental Ni−Gd system, assuming that the slight structural variations due to other f ions are not affecting the semiquantitative conclusions. We performed Complete Active Space Self Consistent (CASSCF) and Density Functional Theory (DFT) calculations (with B3LYP functional), carrying out certain nonstandard operations, as explained in the results and discussion sections. The spin−orbit calculations (SO) performed with CASSCF wave functions accounted for the magnetic anisotropy of lanthanide ions. Extracting extra-output from the black box of the computation, namely, the matrix elements of the L_x, L_y, and L_z operators, we retrieved the orbital components of the Zeeman Hamiltonian which, aside of the trivial spin-type Zeeman part, enabled the explicit implementation of the magnetic field dependence in the CASSCF-SO matrix. Then, for each state i from the CASSCF-SO spectrum, one may express the derivative with respect of the field B and its orientation determined by the θ, φ polar coordinates: $M_i(\theta,\varphi) = -(dE_i/dB)_{\theta,\varphi}$. This quantity has the meaning of a state-specific magnetization, the macroscopic magnetization being a statistical average over such components. With explicit dependence of the field magnitude and orientation, the sum of the state can be worked out, $Z(\theta,\varphi,B) = \sum_i \exp(-E_i(\theta,\varphi,B)/k_BT)$, staying at the basis of ab initio simulation of magnetic susceptibility, using the generic formula $\chi(\theta,\varphi) = d^2 \ln(Z(\theta,\varphi,B)/dB^2)$. The anisotropic susceptibility is averaged over the all possible orientations $\overline{\chi} = (1/4\pi)\int_{\theta=0}^{\theta=\pi}\int_{\theta=0}^{\theta=2\pi} \chi(\theta,\varphi) \sin(\theta)\, d\theta\, d\varphi$. The derivatives involved in the mentioned procedures are performed numerically, with a dB = 0.001 T increment, the integration from last formula being estimated as a double sum over a a 24 × 48 mesh on the θ, φ angles.

3. RESULTS AND DISCUSSION

3.1. Structure Description. The structural determination of the Ni−Yb complex **4** (Figure 1) confirms that we are dealing with a dinuclear Ni−Yb entity in which the nickel ion occupies the inner N_2O_2 coordination site and the Yb ion the outer O_2O_2 coordination site of the compartmental ligand. The two metal ions are bridged by the two deprotonated phenoxo oxygen atoms, and the four NiO_2Yb atoms are almost coplanar, the dihedral angle between the NiO1O2 and YbO1O2 planes being equal to 2.58(6)°.

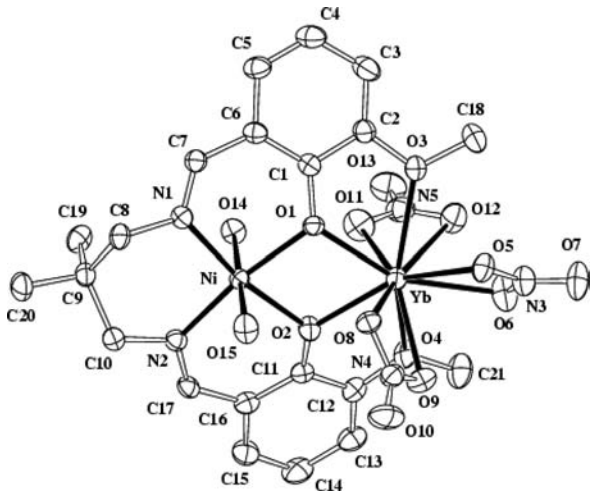

Figure 1. Plot of the asymmetric unit for **4** with the ellipsoids drawn at the 30% probability level and hydrogen atoms suppressed for clarity. Selected bond lengths (Å) and angles (deg): Ni N1 2.001(3), Ni N2 2.011(3), Ni O1 2.032(2), Ni O2 2.029(2), Ni O14 2.159(3), Ni O15 2.132(3), Yb O1 2.267(2), Yb O2 2.239(2), Yb O3 2.484(3), Yb O4 2.504(3), Yb O5 2.496(2), Yb O6 2.418(3), Yb O8 2.406(2), Yb O9 2.424(3), Yb O11 2.366(3), Yb O12 2.940(6), O1 Ni O2 77.61(9), O1 Yb O2 68.77(8), Ni O1 Yb 106.22(10), Ni O2 Yb 107.33(10).

The central core of the molecule is characterized by very similar Ni−O(i) (i = 1, 2) bond lengths (2.029(2) and 2.032(2) Å), slightly different Yb−O(i) bonds (2.239(2) and 2.267(2) Å) and Ni−O(i)−Yb angles of 106.2(1) and 107.3(1)°, giving a Ni−Yb distance of 3.4410(6) Å. The nickel ion is in an octahedral environment, the N_2O_2 atoms of the ligand defining the equatorial plane while two oxygen atoms of water molecules occupy the apical positions with longer Ni−O bonds (2.132(3) and 2.159(3) Å) than those from the equatorial moiety. There are two intramolecular hydrogen bonds between water molecules and the nearest nitrato oxygen atoms, $O(w14)H_2\cdots O11$ and $O(w15)H_2\cdots O8$. The Ytterbium ion is nonacoordinate, four oxygen atoms coming from the ligand and five from the three nitrato ions, two chelating and one monodentate ions. As usual, the methoxy bonds are slightly larger than the nitrato bonds.

A selection of the main bonds and angles is given in the caption of Figure 1. The Shape program[23] allows to define the Yb environment as being the spherical capped square antiprism ($S_{CSAPR\text{-}9}$ = 2.37) while the nickel ion is in a practically perfect octahedron (S_{Oh} = 0.47). Although this molecule has no chiral center, it crystallizes in the non centrosymmetric $P2_1$ space group. The molecule is not planar, the ligand being in a non symmetric boat conformation with the phenyl cycles making dihedral angles of 14.6(1) and 23.8(1)° with the N_2O_2 equatorial plane. To keep a practically planar Yb−O_2−Ni core, the o-vanillin ligands (ovan) are not folded in the same way, so that a two-winged propeller-like conformation appears. This is particularly well shown if we look at the oxygenated part of these ovan ligands surrounding the Yb ion. From the ORTEP drawing, we can see that we have a two-winged right-handed propeller structure. Then these molecules undergo head-to-head stacking to eventually form chiral crystals. In a column, the molecules are linked by hydrogen bonds involving the water molecule $O(w15)H_2$ and the non coordinated O13 oxygen of a nitrato ion. These columns are linked together by hydrogen bonds implying the other water molecule $O(w14)H_2$ and the nitrato O5 oxygen atom coordinated to the Yb ion. The unit cell contains two molecules that are at the origin of two columns oriented in opposite direction. In columns having the same orientation, the intracolumn distance between the metal ions is equal to 10.020(1) Å while the intercolumn distance is shorter, 8.8542(10) Å. Two columns of opposite orientation interact owing to $\pi-\pi$, CH-π, and CH···O contacts, C17···C5, C13···CH(8B), CH(8A)···O9, CH(17)···O10, CH(4)···O7, so that the Ni···Ni and Yb···Yb distances are respectively equal to 8.2159(8) and 10.9298(9) Å. In the present case, we have a chiral crystallization which gives only one enantiomorphic crystal in a 100% yield, contrary to the spontaneous resolution of a racemic compound that undergoes separation of both enantiomers from solution.

Powder XRD studies[24] of the equivalent Ni−Tb **1**, Ni−Dy **2**, Ni−Er **3** molecules confirm that they do crystallize in the same $P2_1$ space group. Their cell parameters are reported in Table 1, along with the previously published Ni−Gd complex.[1] They confirm the isostructurality of this series going from Gd to Yb. In the case of Yttrium, which is assimilated to a rare earth, the Ni−Y complex does also crystallize in the same non centrosymmetric space group.[25]

The structural determination of the Zn−Ho complex **5** presents similar characteristics, so that only differences are

dx.doi.org/10.1021/ic3001784 | Inorg. Chem. 2012, 51, 11279−11293

Table 1. Cell Parameters for Different Ni-Ln Complexes

complex	a (Å)	b (Å)	c (Å)	β (deg)
Ni–Gd[a]	10.1351(6)	16.079(2)	8.8948(9)	91.138(7)
Ni–Tb[b]	10.1275(7)	16.097(1)	8.9002(7)	91.117(1)
Ni–Dy[b]	10.030(7)	15.94(1)	8.853(7)	91.05(1)
Ni–Er[b]	10.005(3)	15.960(6)	8.856(3)	90.948(5)
Ni–Yb[a]	10.0202(11)	15.9443(14)	8.8542(10)	90.942(13)

[a]XRD data. [b]Powder XRD data.

pointed out (Figure 2). The space group is centrosymmetric, with two molecules in the unit cell. The zinc ion is

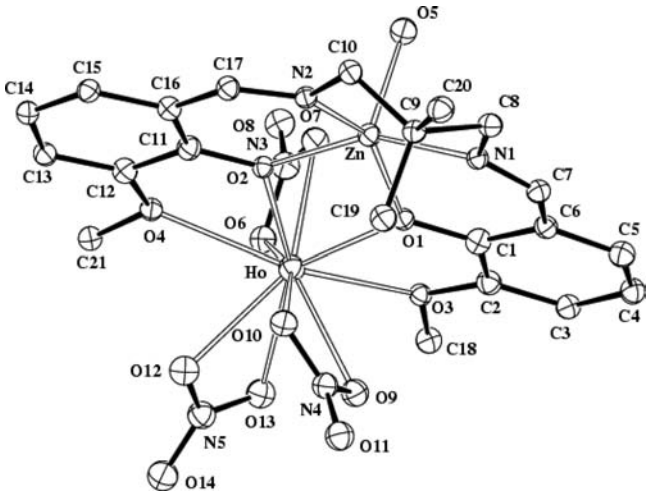

Figure 2. Plot of the asymmetric unit for **5** with the ellipsoids drawn at the 30% probability level and hydrogen atoms suppressed for clarity. Selected bond lengths (Å) and angles (deg): Zn N1 2.088(2), Zn N2 2.032(2), Zn O1 2.042(2), Zn O2 2.057(2), Zn O5 2.057(2), Ho O1 2.268(2), Ho O2 2.293(2), Ho O3 2.495(2), Ho O4 2.525(2), Ho O6 2.450(2), Ho O7 2.485(2), Ho O9 2.480(2), Ho O10 2.480(2), Ho O12 2.469(6), Ho O13 2.578(2), O1 Zn O2 75.99(8), O1 Ho O2 67.16(7), Zn O1 Ho 109.06(8), Zn O2 Ho 107.59(8).

pentacoordinate with one water molecule in axial position, with slightly larger Zn–N and Zn–O bonds, except for the Zn–O(w5) involving the water molecule. The ligand frame is more planar, with the Zn ion above the mean plane of the donor atoms and the Ho ion below that plane and a Zn···Ho distance of 3.5131(6) Å. This arrangement induces a slightly larger dihedral angle between the Zn–O1–O2 and Ho–O1–O2 planes (4.03(9)°). A unique hydrogen bond between the water molecule and an acetone molecule of crystallization is observed. The centrosymmetry introduces larger Zn···Zn (10.6324(11) Å) and Ho···Ho (11.5372(13) Å) distances while the shorter Zn···Zn and Ho···Ho distances between molecules are equal to 9.684(1) Å.

3.2. Magnetic Properties. The magnetic susceptibilities of the four Ni-Ln complexes **1**–**4** (Ln = Tb, Dy, Er, Yb) have been measured in the 2–300 K temperature range under an applied magnetic field of 0.1 T. The thermal variation of the $\chi_M T$ product for complex **1** is displayed in Figure 3a, χ_M being the molar magnetic susceptibility of the dinuclear species, corrected for the diamagnetism of the ligands. At 300 K, $\chi_M T$ is equal to 13.3 cm^3 mol^{-1} K. Lowering the temperature results in a slow $\chi_M T$ decrease down to 50 K (12.9 cm^3 mol^{-1} K) followed by an abrupt increase, up to 14.5 cm^3 mol^{-1} K at 7 K and a slight decrease to 14.3 cm^3 mol^{-1} K at 2 K. This behavior indicates that a ferromagnetic interaction between the Ni^{II} (S = 1) and Tb^{III} (J = 6) ions operates at low temperature.

A similar behavior is observed for complex Ni–Dy (compound **2** in Figure 3b), with a slight $\chi_M T$ decrease from 300 (14.74 cm^3 mol^{-1} K) to 40 K (14.20 cm^3 mol^{-1} K), followed by an increase until 7 K (15.34 cm^3 mol^{-1} K) and a steep decrease to 13.5 cm^3 mol^{-1} K at 2 K. These behaviors are different from those observed in the Ni–Er and Ni–Yb samples. For complex Ni–Er (compound **3**), $\chi_M T$ equals 11.8 cm^3 mol^{-1} K at 300 K (Figure 4a), followed by a smooth $\chi_M T$ decrease to 10.9 cm^3 mol^{-1} K at 100 K, a more pronounced decrease until 20 K (9.0 cm^3 mol^{-1} K) and a steeper decrease to 7.5 cm^3 mol^{-1} K at 2 K. In the case of Ni–Yb (compound **4**), the value remains practically constant from 300 K (3.14 cm^3 mol^{-1} K) to 120 K (2.95 cm^3 mol^{-1} K), decreases smoothly to 2.5 cm^3 mol^{-1} K at 20 K and more abruptly to 1.62 cm^3 mol^{-1} K at 2 K (Figure 4b). The values reached at the plateaus of the experimental $\chi_M T$ curves established between 200 and 300 K roughly correspond to the sum of 3d and 4f paramagnets. Analogously to the $0.12505 \cdot g_S^2 \cdot S(S+1)$ estimation for a spin-only system, the lanthanides can be characterized by the $0.12505 \cdot g_J^2 \cdot J(J+1)$ formula, with the Landé factor estimated by the corresponding ideal L, S, and J quantum numbers, $g_J \approx 3/2 + (S(S+1) - L(L+1))/(2J(J+1))$. For the upper branch of the lanthanides, the ground state is given by $J = L + S$. In the given series, the ionic terms, ascribed as $Ln(^{2S+1}[L]_J)$, are as follows: Tb($^7F_6$), Dy($^6H_{15/2}$), Er($^4I_{15/2}$), and Yb($^2F_{7/2}$). The corresponding ideal g_J factors assigned to the groundstates g_{Ln} of the Ln ions are g_{Tb} = 1.5, g_{Dy} = 1.33, g_{Er} = 1.2 and g_{Yb} = 1.14, giving

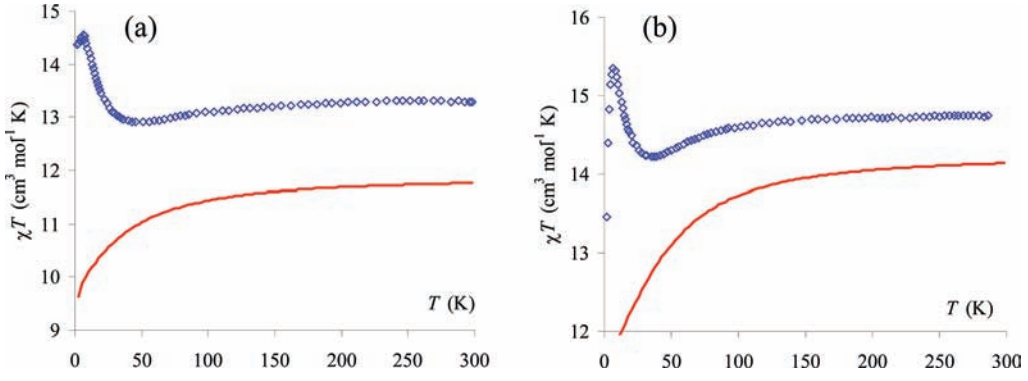

Figure 3. $\chi_M T$ vs T curves for (a) Ni–Tb and (b) Ni–Dy complexes. The marked points (blue diamonds) correspond to the experimental data. The continuous lines (red) show the ab initio simulation of the lanthanide only (done on Zn–Tb and Zn–Dy complexes).

dx.doi.org/10.1021/ic3001784 | Inorg. Chem. 2012, 51, 11279–11293

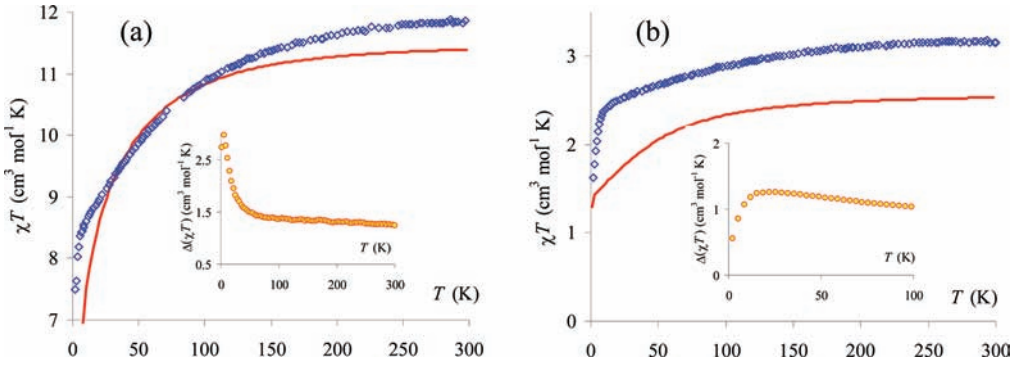

Figure 4. $\chi_M T$ vs T curves for (a) Ni−Er and (b) Ni−Yb complexes. The marked points (blue diamonds) correspond to the experimental data. The continuous lines (red) show the ab initio simulation of the lanthanide only (done on Zn−Er and Zn−Yb molecules).

rise to the respective paramagnetic contributions to the $\chi_M T$: 11.817, 14.172, 11.479, and 2.572 cm^3 mol^{-1} K units, in correct agreement with our experimental observations.

As a general pattern of the $\chi_M T$ product, the Tb and Dy congeners are similar each to other (see Figures 3a and 3b), showing a low temperature part where the $\chi_M T$ increase because of ferromagnetic Ni-Ln coupling is clearly marked. In turn, the ferromagnetic signature is not directly visible for the Er and Yb systems, the lanthanide orbital degeneracy being able to induce a large $\chi_M T$ decrease at lower T (see Figures 4a and 4b). However, the ferromagnetic coupling is nicely revealed in performing the difference between the $\chi_M T$ values of the concerned **3** and **4** compounds and those measured for Zn−Er **6** and Zn−Yb **7** analogous complexes.

According to a qualitative method described previously,[26] the difference $\Delta\chi_M T = \chi_M T(\text{Ni-Ln}) - \chi_M T(\text{Zn-Ln})$ allows elimination of the crystal field contribution of Ln ions in each pair. The difference curves are presented as insets to the Figures 4a and 4b. So the $\Delta\chi_M T$ value of 1.25 cm^3 mol^{-1} K at 300 K for the Ni−Er/Zn−Er system (Figure 4a) corresponds to the contribution of an isolated nickel ion (1 cm^3 mol^{-1} K is expected with g = 2). This value remains practically constant until 60 K (1.45 cm^3 mol^{-1} K), then increases to 3.04 cm^3 mol^{-1} K at 6 K before decreasing to 2.73 cm^3 mol^{-1} K at 2 K. This behavior does confirm that a ferromagnetic Ni−Er interaction is active at low temperature, while the Zero Field Splitting (ZFS) coming from nickel ions is responsible for the slight decrease below 6 K. A similar analysis based on the Ni−Yb/Zn-Yb system is not so clear (inset of Figure 4b). The $\Delta(\chi_M T)$ curve goes from 0.9 cm^3 mol^{-1} K at 100 K to 1.24 cm^3 mol^{-1} K at 20 K and decreases to 0.58 cm^3 mol^{-1} K at 2 K. If the Ni ZFS appears clearly in the 2−10 K temperature region, the $\Delta(\chi_M T)$ increase in the 50−20 K temperature range plays in favor of a weak Ni−Yb ferromagnetic interaction, surely weaker than in the Ni−Er complex. Although the Ni-Ln and Zn-Ln families do not crystallize in the same space group, a look at the Ln coordination spheres with the SHAPE program[21] does confirm that the Gd and Ho ions are best described as having a sphenocorona environment ($S_{\text{JSPC-10}}$ = 2.66 and 2.48 for the Ni−Gd and Zn−Ho complexes, respectively). A similar value is obtained with the Ni−Yb entity if we take into consideration the tenth oxygen atom located at 2.940(6) Å ($S_{\text{JSPC-10}}$ = 2.63), which justifies the use of the qualitative $\Delta(\chi_M T)$ difference. The occurrence of ferromagnetic interactions along the Ni−Gd to Ni−Yb series is in line with previously expressed qualitative expectations,[27] being consistently supported by ab initio calculations presented in the next sections.

The Figures 3 and 4 contain the experimental data as marked points (diamond symbols) while the continuous curves correspond to the computed ab initio lanthanide contribution (using Ni-Ln models in which the transition metal is replaced by Zn), anticipating in this way the advances presented in the modeling sections. These curves clearly highlight the role of lanthanide ions in the $\chi_M T$ decrease at low temperature.

To find out whether our compounds show SMM behavior, we performed alternating current (ac) susceptibility measurements in the 2−6 K range using a MPMS SQUID magnetometer with a zero direct current (dc) field and a 3 Oe ac field oscillating at 10−1000 Hz. No out of phase susceptibility signal was observed in the absence of an applied magnetic field. It has been previously shown that trinuclear W-Ni-Ln and hexanuclear W-Ln-Ni-W-Ni-Ln complexes exhibit out of phase χ''_M signals when the starting Ni-Ln complexes are devoid of such signals in absence of an applied magnetic field.[28] On the contrary, a frequency-dependent decrease in the in-phase (χ'_M) susceptibility signal along with a concomitant increase of the out of phase (χ''_M) susceptibility signal were observed for the complexes **1**, **2**, **3**, and **4** in presence of an applied static field of 1000 Oe. The profile of these curves (Figures S1−S3 in Supporting Information) is characteristic of a SMM, while the absence of χ''_M signals at zero field indicates that quantum tunnelling is active. The χ''_M maxima were used to determine the relaxation rates τ. Arrhenius plots of $\ln(\tau)$ vs $1/T$ allowed to find the effective energy barriers U_{eff} and the pre-exponential factors τ_0 in the four complexes. These values are respectively found equal to 13.0, 21.0, 20.1, 20.8 K for U_{eff} and 1.38×10^{-6}, 8.77×10^{-8}, 7.13×10^{-9}, 4.5×10^{-9} s for τ_0 in complexes **1**−**4**. Observation of χ''_M signals for the Ni−Er and Ni−Yb complexes is surprising and seems to indicate that the Ni contribution to the anisotropy must be effective. Indeed, if such a behavior was previously observed for other Ni−Tb and Ni−Dy samples,[29] it is observed for the first time in the Ni−Er and Ni−Yb complexes. The corresponding Zn−Er and Zn−Yb complexes are devoid of χ''_M susceptibility signals, indicating that the SMM behavior is a property characteristic of the Ni-Ln pair for it cannot be induced by the Ln ion alone. Because of the large separation of the Ni-Ln molecules, the observed magnetic behavior is an intramolecular property. As fast quantum tunnelling seems active in these compounds, we have not performed magnetization hysteresis loop measurements using a micro-SQUID apparatus to confirm their SMM properties.

dx.doi.org/10.1021/ic3001784 | Inorg. Chem. 2012, 51, 11279−11293

3.3. Multiconfiguration Ab Initio Calculations: the d-f Exchange Coupling and Ligand Field Effects. As pointed out in the introductory part, the modeling of magnetic properties, in general, and the account of quasi-degenerate ground states of lanthanide ions can be achieved properly only by multiconfiguration methods. Here we used the Complete Active Space Self Consistent Field (CASSCF) method, followed by spin−orbit (SO) treatments, to account for the magnetic anisotropy. An essential strategy, established by our previous methodological finding is to initiate the CASSCF iterations with a wave function prepared by merging the orbital coefficient matrices in a block that has zero elements between the constituting fragments. Thus, to calculate a $(H_2O)_2$NiL-Ln$(NO_3)_3$ complex, we had three blocks prepared in advance by the separate calculations of the $(H_2O)_2$NiL complex moiety, the nitrato set $(NO_3^-)_3$ and the free lanthanide ion Ln^{3+}. This initial selection answers well to the sensitivity of the CASSCF to the choice of so-called active space (the orbitals and the number of contained electrons, all the possible configurations being considered inside this set). Thus, the key consists in the insertion of pure f orbitals in the active space, aside from the selected set belonging to the d complex unit.

For Ni-Ln complexes with f^n lanthanide ions we performed CAS(n+2,9) calculations (i.e., n+2 electrons in 9 orbitals), considering an active space made of the two SOMOs (Single Occupied Molecular Orbitals) from Ni(II) and the seven f orbitals, the total occupancy, n + 2, being given by the two unpaired electrons from the d center plus the n electrons of the f site.

Even though not belonging to the current set of complexes, the first characterized system is the Ni−Gd complex,[1] to have a clear reference for the case without orbital quasi-degenerate regime on the lanthanide. We calculated the exchange coupling constant using different technical settings. The CASSCF(9,9) which belongs to the previously mentioned CAS(n+2,9) standard, yielded J_{NiGd} = 0.678 cm^{-1}. Here we use the $-2J\hat{S}_1\cdot\hat{S}_2$ convention of the spin Hamiltonian. The calculations with an enhanced active space, CASSCF(15,12), including all the 15 electrons in 12 orbitals originating from the d^8+f^7 set, yields approximately the same amount, J_{NiGd} = 0.638 cm^{-1}. This illustrates that the doubly occupied components of the d^8 ion are not collaterally implied in the exchange effect, and we can confine in the following to the simpler choice of active space. Considering that the CASSCF can be suspected in certain circumstances of lacking the so-called dynamic correlation effects,[30] we performed, a posteriori to the CASSCF(9,9) calculation, the multireference second order perturbation (MRPT2), as implemented in the used GAMESS code.[31] One observes then the increase of the magnitude of estimate exchange to J_{NiGd} = 0.915 cm^{-1}. The experimentally fitted value[1] is J_{NiGd}^{exp} = 1.56 cm^{-1} (in original work, considering a different Hamiltonian convention, $-J\hat{S}_1\cdot\hat{S}_2$, the value is J_{NiGd}^{exp} = 3.13 cm^{-1}).

The CASSCF accounts semiquantitatively for the sign and the order of magnitude of the exchange parameter, the MRPT2 corrections shifting the value closer to the experimental estimation. Because the second order increments are quite demanding of the computing resources, we consider the semiquatitative performance of the actual CASSCF setting as sufficient to realistically retrieve the mechanism factors. The CASSCF calculations allow the estimation of Ligand Field effects on the f shell, via the computed split of the levels assignable to the ground terms, $^{2S+1}[L]$, in accordance to the corresponding L and S quantum numbers of each ion. Table 2 presents the corresponding terms computed for the **1**−**4** systems.

Table 2. Levels Assignable to the Ligand Field (LF) Split Components of the Lanthanide Ground Terms, Collected from States with Higher Spin Multiplicities[a] in CASSCF Calculations of Ni-Ln Complexes

split atomic terms	ΔE_{LF} (cm^{-1})			
$^{2S+1}[L]$ Ln	^7F Tb	^6H Dy	^4I Er	^2F Yb
1	0.0	0.0	0.0	0.0
2	104.3	19.9	21.6	137.0
3	224.0	79.3	86.1	175.5
4	271.3	91.8	112.8	241.6
5	284.2	189.7	147.7	266.6
6	440.3	236.5	200.3	392.7
7	675.6	266.7	220.2	463.8
8		302.3	237.2	
9		413.5	262.3	
10		445.8	317.9	
11		508.0	328.8	
12			376.7	
13			391.4	

[a]Ferro-type spin coupling.

A simple relationship of computed terms with the Ligand Field (LF) scheme exists in the case of the Tb(III) complex. The ^7F term is made from combinations of the seven possibilities to run the β electron over the orbitals of the f^8 shell. Using the so-called canonical orbitals, conventionally labeled f_1, ..., f_7, the i-th level formally originating from the ^7F term on Tb(III) can be expressed by a configuration having the main component with the β electron placed in the f_i function. The orbitals were obtained from the CASSCF(10,9) calculation with S = 9 multiplicity for the Ni−Tb complex. The main component is clearly identified by leading coefficients ranging between 0.90 and 0.99. In such circumstances, the canonical orbitals can be conceived as one-electron f functions diagonalizing an ab initio generated Ligand Field Hamiltonian. The possibility to consider in this way the problem of Ligand Field on f shell circumvents many algebraic complexities or parametric uncertainties that affect a classical approach by a phenomenological Hamiltonian.[32a] The splitting range outlined in Table 2, with about 500−700 cm^{-1} total gaps, is in line with the expectations known for LF on f complexes.[32a] We will not attempt here to decompose these results in a classical scheme, since this implies technical details[32b] that are beyond the current focus.

Table 3 suggests an interesting observation: for each orbital state due to the f ion, one may assign a $J_{df}(\Omega)$ coupling parameter for the interaction of the given lanthanide term (Ω) with the d ion. Performing calculations with different spin multiplicities, belonging to the $|S_{Ln} - S_{Ni}|$, ..., $S_{Ln} + S_{Ni}$ range, we obtain series of 2L+1 levels, each set being close to the values printed in Table 2 (which correspond to the $S_{Ln} + S_{Ni}$ case). Thus, the spacing of levels shows the same Ligand Field pattern at all the spin multiplicities. The small separations of the levels with the same Ligand Field component and different spin multiplicities is due to the exchange effects. One may assign, in this way, exchange coupling parameters, $J_{df}(\Omega)$, for each Ω orbital state of a lanthanide center, repeating for each one the

dx.doi.org/10.1021/ic3001784 | Inorg. Chem. 2012, 51, 11279−11293

Table 3. State Dependent Exchange Coupling Parameters, $J_{df}(\Omega)$, Estimated for Each Component of the Split Lanthanide Ground Terms, $^{2S+1}[L]$[a]

state dependent coupling	$J_{df}(\Omega)$ (cm^{-1})			
$^{2S+1}[L]$, Ln	^7F Tb	^6H Dy	^4I Er	^2F Yb
1	0.641	0.598	0.521	0.598
2	0.618	0.573	0.528	0.341
3	0.603	0.605	0.495	0.360
4	0.639	0.619	0.514	0.454
5	0.567	0.582	0.505	0.532
6	0.614	0.487	0.533	0.362
7	0.554	0.621	0.515	0.241
8		0.528	0.508	
9		0.552	0.496	
10		0.553	0.486	
11		0.543	0.489	
12			0.469	
13			0.461	

[a]Here Ω symbolizes the components resulting from the split of the given $[L]$ orbital multiplet.

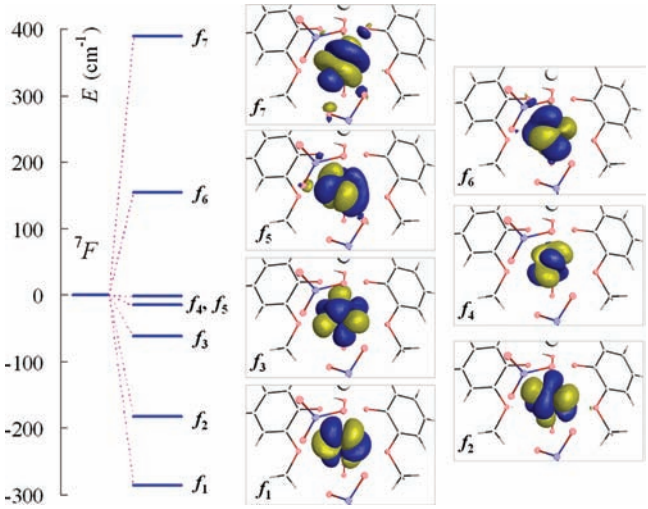

Figure 5. Energy levels from CASSCF calculations on the Ni–Tb complex relevant for the splitting of the ^7F spectral term which effectively accounts the Ligand Field scheme on the f shell. The levels are conventionally shifted to yield a barycenter in the zero point. The depicted orbitals represent the one-electron effective functions assignable to the computed levels.

Heisenberg formalism. It is observed that all the state-dependent coupling parameters, $J_{df}(\Omega)$, show closely similar ferromagnetic values. This information is nontrivial and can be taken as a stable approximate feature of the exchange mechanism. The quasi-equality of exchange splitting on all the states resulting from a LF lanthanide multiplet suggests that all the involved individual configurations (Slater determinants) show also mutually close exchange parameters. The exchange coupling parameter of each configuration is modulated by its composition as a combination of Slater determinants. If all the configurations (and therefore Slater determinants that serve as multiconfiguration basis) show similar coupling parameters, this means that the d-f exchange is not affected directly by orbital effects, such as the overlap and kinetic exchange. The ferromagnetic interaction is then induced by a mechanism similar to the one previously discussed in the Cu–Gd prototypic system, which is basically free of overlap incidence.[5] The orbital promotions from the SOMOs of 3d complex to the empty 5d AOs (or equivalently, the incorporation of 5d delocalization tails in the canonical MOs) are tuning the parallel coupling of the spins from the d and f moieties. The interaction of residual spin densities located in 5d AOs with the spin of the f terms is determined by one-center exchange effects, the overall mechanism being, in this way, less dependent from formal intercenter overlapping. This is in line with the closeness of the $J_{df}(\Omega)$ values in Table 3. Another consequence of this pattern is the following: if the coupling constants are quasi-equal, then there are reasons to think about a $-2J_{df}\hat{S}_d\cdot\hat{J}_f$ analogue of the $-2J_{df}\hat{S}_1\cdot\hat{S}_2$ spin Hamiltonian with the $\hat{J}_f$ angular momentum replacing the spin operator on the f site. This is because the equal exchange parameter can be factored from each configuration and since these are mutually mixing according to *LS* coupling algebra, the resulting *J* quantum numbers are replacing the *S* ones. We keep this statement as mere guess or suggestion, without entering algebraic proofs. However, because the lanthanides are never free of SO coupling, the phenomenology of $\hat{S}_d\cdot\hat{J}_f$ coupling cannot be, in fact, found in real problems. In turn, an Ising-like mutation of such expression can be assumed with exchange, LF and SO included, as suggested by the considerations from the 3.5 paragraph.

3.4. Ab Initio Account of the Magnetic Anisotropy on Lanthanide Centers. The description of local effects on lanthanides is completed including the spin–orbit (SO) elements which give rise to a further splitting of each element from the LF-type sequence of orbital states. Or, conversely, if we rely on the free ion with SO included, the LF causes the split of each *J* term resulting from the *LS* vector coupling.

This situation is illustrated in Figure 6 for the Tb(III) ion, whose free-ion ground term corresponds to the $J = 6$ quantum

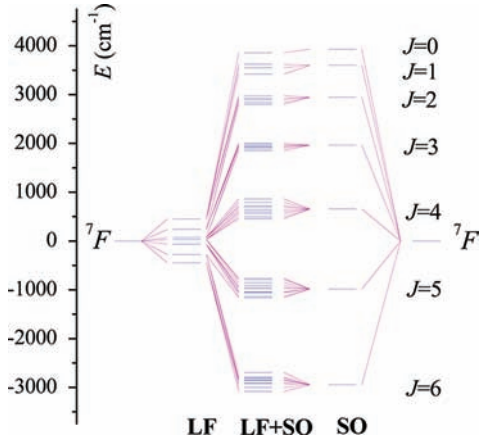

Figure 6. Ab initio simulation of combined Ligand Field (LF) and Spin Orbit (SO) effects determining the local electronic terms of the Tb(III) embedded in the complex. The calculations were done on the hypothetical $[(H_2O)_2ZnL\text{-}Tb(NO_3)_3]$ complex. The right side levels (marked by SO) were done on the free Tb(III) ion, where only SO effects are active. The splits marked by LF correspond to the levels detailed in Figure 5. The levels in the middle of the graph were obtained by CASSCF-SO that reproduce the LF+SO regime. All data sets were conventionally shifted to a zero barycenter.

number, $^7F_6$. The Ligand Field induces a split of the $J = 6$ components into a series of almost degenerate couples, formally assignable to the non-null $\pm J_z$ components and a nondegenerate level originating from $J_z = 0$. Thus, the first four levels (0.0, 0.5, 82.7, 84.5 cm^{-1}) are arranged in two

dx.doi.org/10.1021/ic3001784 | Inorg. Chem. 2012, 51, 11279–11293

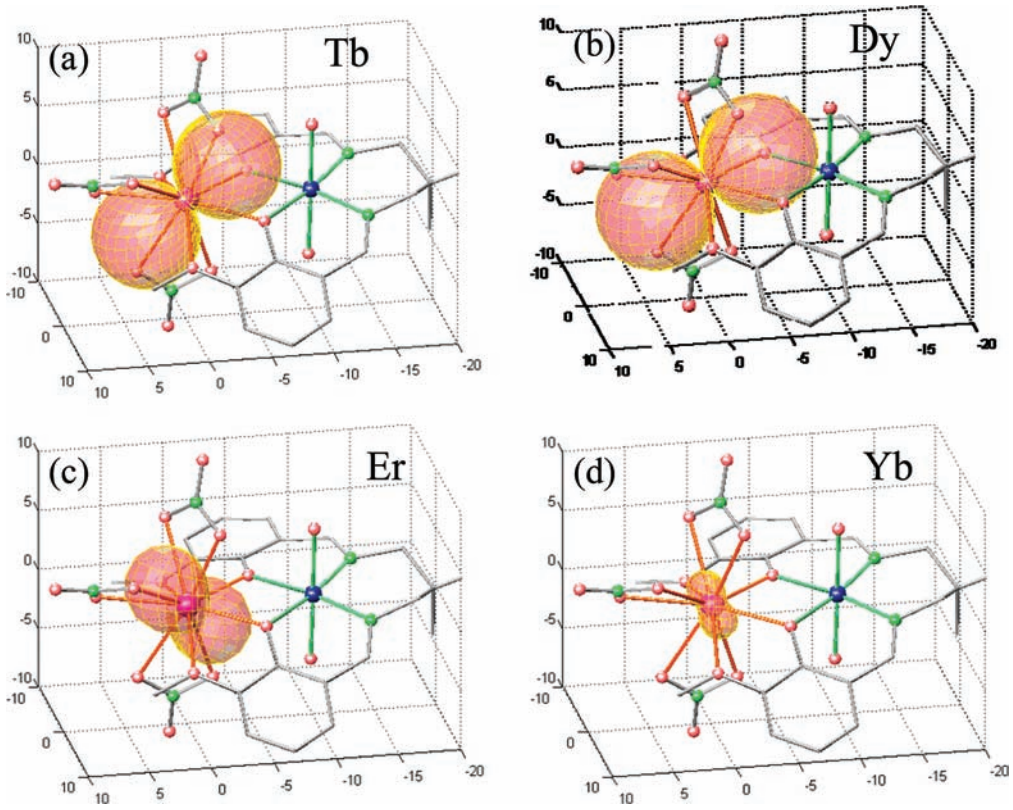

Figure 7. Polar diagrams of state-specific magnetization functions, $M = |dE/dB|$, for the ground state components of the Ln = Tb, Dy, Ho, Er complexes. The calculations are done on $[(H_2O)_2ZnL\text{-}Ln(NO_3)_3]$ complexes. The complete drawings of all the state-specific $M_i = |dE_i/dB|$ functions for all the representative states of the $2J + 1$ ground multiplets of the considered ion are given in the Supporting Information.

quasi-degenerate pairs, with a ground state doublet well separated from the next elements (see Table S1 in Supporting Information). The last two quasi-doublets appear at 386.5, 386.9 cm^{-1}. The energy gap in the 10^2 cm^{-1} scale explains the continuous variation in the experimental $\chi_M T$ vs T curves over the 0−300 K, in agreement with a progressive population of the magnetic states due to the lanthanide ion. The fact that the data resulting from such calculations yielded (with the handling explained in the technical section) theoretical curves parallel to the experimental patterns (see Figures 3, 4) validates the capacity of the actual theoretical methodology for semiquantitative accounts.

For the other Ln ions in the Ni-Ln series (see Tables S1−S4 from Supporting Information), the CASSCF-SO calculation on lanthanide ions (using $[(H_2O)_2ZnL\text{-}Ln(NO_3)_3]$ systems), the computed levels result in series of perfectly degenerate pairs, recalling again the suggestion of $\pm J_z$ correspondence. The regularity is imposed by the symmetry of the half integer J quantum numbers corresponding to the ground states of Dy, Er, Yb, that is, J = 15/2, 15/2, and 7/2. Comparatively, the previously discussed Tb(III) case with an integer $J = 6$ quantum number, resulted in only a quasi-degenerate pattern.

The analogy of the spectral pattern with the $\pm J_z$ series is not completely satisfactory, since the momentum projections are not good quantum numbers in an asymmetric environment. Valuable information about the magnetic features of each state can be realized by further handling of the ab initio Hamiltonian. We propose an illustrative way of interpretation, by drawing the polar diagrams of the functions called state-specific magnetizations.[33]

If the field dependence in the full ab initio Hamiltonian is introduced (see technical section at the end of Experimental Section), the magnetization of the *i*-th level can be obtained as the derivative of the corresponding *eigenvalue* with respect of the field: $M_i = -dE_i/dB$. Representing the polar diagrams of the response functions $M_i(\theta,\varphi)$ of the Hamiltonian, according to the magnetic field applied in various orientations, as a function of θ and φ polar coordinates, we obtain a visual and suggestive description of the magnetic anisotropy of the *i*-th state of the given ion in its actual LF environment.

The Figure 7 shows the ground state specific magnetizations for the Tb, Dy, Er, and Yb complexes. The construction of the $M_i(\theta,\varphi)$ polar diagram has the following principles: consider a direction determined by θ and φ polar angles, apply an infinitesimal perturbation by the dB field, estimate the derivative $M_i = -dE_i/dB$, and then find the point determined by the $|M_i|$ radius along the (θ,φ) direction, which must be considered as a dot on the desired surface. The surfaces are drawn repeating this algorithm over a mesh of polar coordinates, similar to the latitude and longitude specifications on a globe map. The extension of the surface in a given space orientation determines the sensitivity of the selected state to a field applied from that direction. The directions showing the maximal extension correspond to the easy magnetization axes for the given states. For the couples showing exact degeneracy, as it happens for the Dy, Er, and Yb complexes, the degenerate functions show identical polar diagrams. Even for the Tb system, showing only approximate double degeneracy pairing, the polar diagrams of closely related levels are similar to each other.

dx.doi.org/10.1021/ic3001784 | *Inorg. Chem.* 2012, 51, 11279−11293

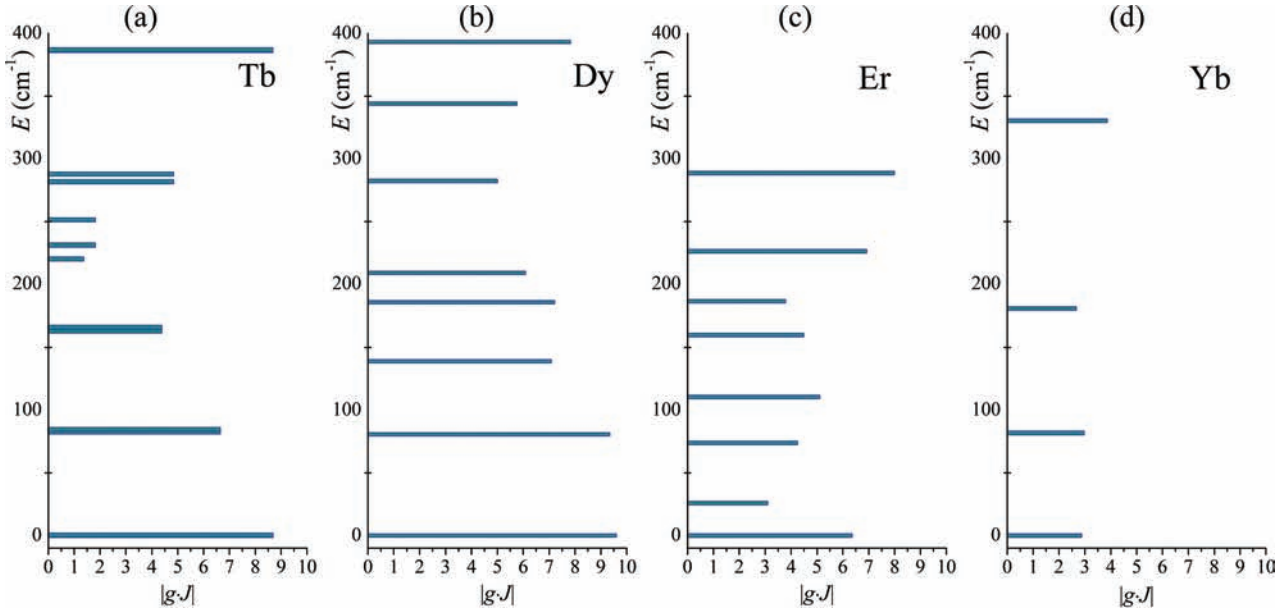

Figure 8. Energy levels from CASSCF-SO calculations corresponding to the LF split of ground J multiplets computed for lanthanide ions in $[(H_2O)_2ZnL\ Ln(NO_3)_3]$ complexes: (a) Tb(III), $J = 6$; (b) Dy(III), $J = 15/2$; (c) Er(III), $J = 15/2$; (d) Yb(III), $J = 7/2$. The bar lengths in abscissa represent the maximal extension of the polar diagrams of state-specific magnetizations, $M_i = |dE_i/dB|$.

The Figure 7 represents the polar diagrams of ground state magnetizations of the considered systems **1**−**4** (see Figures S4−S7 in the Supporting Information, containing the full sets of $M_i(\theta,\varphi)$ functions, for all representative multiplet components of each complex). The polar diagrams contain rich information about the anisotropy of each state, that cannot be easily considered in other manner. The ab initio route generating these valuable functions represents a nontrivial advance in describing the intricacies related to the lanthanide anisotropy issues.

If the z axis is conventionally aligned to the lobe of a given state specific magnetization, the maximal extension of the represented surface can be correlated with the $|g_J J_z|$ effective value. Then, assuming the ideal g_J for the given ion, one may infer the effective value of a J_z. This interpretation has limitations because, first, J_z projections are no longer good quantum numbers if symmetry is lower than axial. Besides, because the lobes of $M_i(\theta,\varphi)$ functions are not aligned, and then, one cannot use a common z axis to quantify all states by J_z-alike quantities extracted from computed $|g\cdot J|$ maximal extensions. However, the maximal extension of state-specific magnetization is an important magnitude to characterize a given level from the representative sequence.

The Figure 8 represents the LF split of the levels resulting from groundstate J multiplets of the ions in the complexes **1**−**4**, with the $|g\cdot J|$ maximal extensions figured by the length of the bars along the abscissa. The numeric data corresponding to these representations are given in the Supporting Information (Tables S1−S4). One observes a general $|g\cdot J|$ vs E nonmonotonic pattern illustrating that the magnetic anisotropy of lanthanide ions is a complicated topic that cannot be treated by a simplified methodology, that is, as is the Zero-Field Splitting Hamiltonian, useful for describing the anisotropy on many transition metal ions.

If an ideal Landé factor is assumed for Tb^{III}, that is, $g_J = 3/2$, the $|g\cdot J|$ found for the first two quasi-degenerate couples suggest their assignments to the $J_z \approx \pm 6$ and $J_z \approx \pm 5$ elements. The next components are too admixed and also show different quantization axis, to be assigned individually in the same manner. However, a visible nondegenerate element can be considered as resulting from the $J_z = 0$ element, in spite of the fact that the $|g_J J_z|$ is not completely vanishing, but being the minimal one (See the line above 200 cm^{-1} tick label in Figure 8a and the element {7} in Figure S4 or line 7 in Table S1, in Supporting Information).

For the Dy(III) complex (with free ion, $g_J = 4/3$), one may assign the lowest two doublets as mutual admixture of the $\pm 15/2$ and $\pm 13/2$ components. In both the above systems the ground state is suggested as related to the maximal J_z projection of the given multiplet and the next level related to the immediate lower indices, while the rest of the spectrum is of nonmonotonic nature (See Figure 8b and Table S2 in Supporting Information).

Following the same approximation of ideal g_J numbers dividing the maximal extension of ground state specific magnetization, the Er and Dy complexes seem to be characterized by the following ground J_z values: about $\pm 11/2$ for Er(III) and approximately $\pm 5/2$ for Yb(III), that is, smaller than the maximal projections, $\pm$ 15/2 and $\pm 7/2$, respectively. The states related with the maximal projection correspond to highest levels (see Figure 8, panels b and c). Such overall distinguishing features can be related with the different $\chi_M T$ vs T behavior recorded for the Tb and Dy complexes, compared to the Er and Yb analogues, as exposed in the experimental part. In the Tb and Dy complexes one observes that, in spite of having different characterization by L, S, and J formal quantum numbers, the polar diagrams of the $M_i(\theta,\varphi)$ functions for ground state elements are similar (see Figure 7) and that, at the same time, the pattern of the levels diagrams from (a) and (b) panels of Figure 8 are mutually similar. In this way, one may qualitatively explain why the Tb and Dy complexes showed similar patterns in the experimental $\chi_M T$ vs T curves and, on the other hand, why they are different for the Er and Yb cases.

3.5. Calculation and Phenomenology of the Anisotropic d-f Exchange. In the above analyses the electronic structure and magnetic properties of the lanthanide center were

dx.doi.org/10.1021/ic3001784 | Inorg. Chem. 2012, 51, 11279−11293

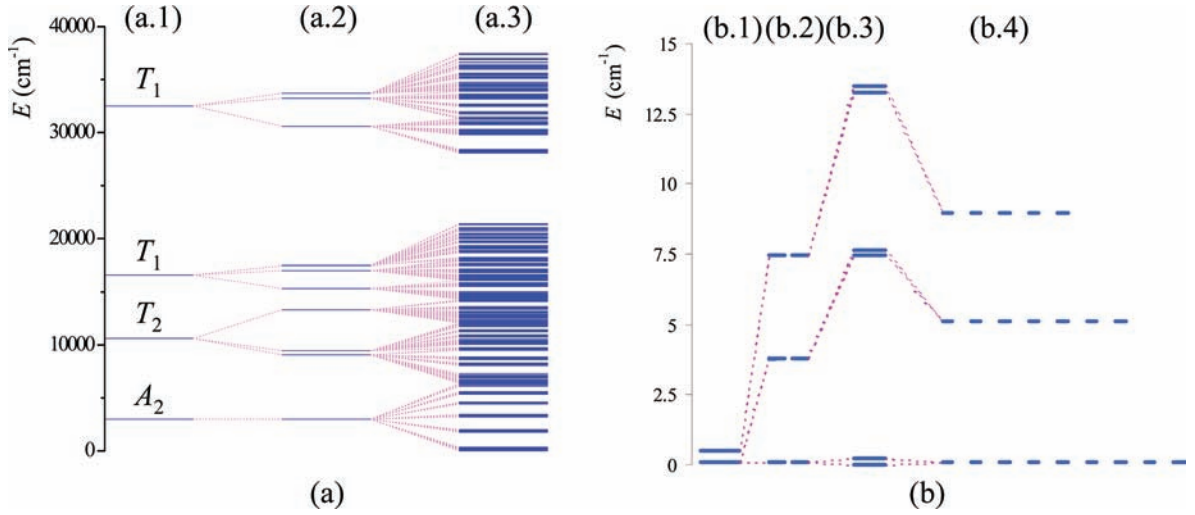

Figure 9. CASSCF-SO spectrum of states at (a) large scale and (b) focused on the ground state sequence. The (a) panel illustrates the parentage with respect of Ni(II) LF states as follows: (a.1) the idealized octahedral Ni(II) reference obtained by the average states corresponding to excited triplets of the d^8 scheme in the actual ligand field, illustrated in (a.2) via CASSCF calculations on the $[(H_2O)_2NiL]$ complex; the (a.3) panel comprises the full series of states from extended multiconfiguration spin−orbit calculations on $[(H_2O)_2NiL\text{-}Tb(NO_3)_3]$ system, accounting for LF and SO effects on both Ni(II) and Tb(III) sites and their mutual exchange coupling. The (b) panel illustrates the ground state sequence resulting from different computation experiments: (b.1) the quasi degenerate doublet due to LF-SO on Tb(III), from CASSCF-SO calculation on the $[(H_2O)_2ZnL\text{-}Tb(NO_3)_3]$ model; (b.2) the Ising-like sequence resulting from CASSCF-SO calculations that accounted SO effects on Tb(III) only, not on Ni(II), from CASSCF-SO calculations including only SOMO components on Ni(II) and the f^8 shell on Tb(III); (b.3) the quasi-Ising like sequence resulting from extended multiconfiguration calculations (with the d^8+f^8 active space) including SO on both Ni(II) and Tb(III); (b.4) the isotropic Heisenberg-like sequence resulting from CASSCF calculations without SO effects.

done switching off the exchange coupling, by considering the $[(H_2O)_2ZnL\text{-}Ln(NO_3)_3]$ hypothetical complexes instead of the true $[(H_2O)_2NiL\text{-}Ln(NO_3)_3]$ systems.

The exchange coupling effects discussed in the section 3.3 do not include the spin−orbit effects. A further step is accomplished by CASSCF(n+2,9)-SO procedures, that is, with active spaces considering only two SOMOs of Ni(II), the f^n shell, and the spin orbit effects. In this case, the SO effects account in fact only for the anisotropy of the lanthanide site, since the corresponding effects on Ni(II) imply the account of full d^8+f^n active space, by CASSCF(n+8,12)-SO calculations. These calculations are very demanding because they cannot be limited to a sequence of few states but mandatorily include all states responsible for complete LF schemes on both systems.

We will treat in the following only the case of Ni−Tb complex, the understanding of the calculation route and results being realized with help of Figure 9, where the (a) panel suggests the full set of states considered while the side (b) zooms the zone of interest, displaying the sequence around the ground state resulted from several numerical experiments.

The simple CASSCF(10,9) calculations yielded the series of states with spin S = 4, 3, 2 (displayed in the Figure 9.b.4), simulating the situation of isotropic exchange, appearing if SO effects did not exist. The anisotropy due to SO on Tb(III) is suggested by the quasi-degenerate doublet (with a spacing of about 0.5 cm^{-1}) shown in Figure 9.b.1, the next LF-SO levels on Tb(III) being located higher than 80 cm^{-1}. The pattern on Tb(III) modulates the anisotropic exchange, generating a series of six lower states, grouped in three doubly degenerate levels (see Figure 9 b.2), after adding SO effects to the CASSCF-(10,9) calculations of exchange coupling. The next series of levels occur above the 100 cm^{-1}. This calculation implies the merging, by SO elements, of seven orbital states for each of the 9, 7, 5 spin multiplicities (resulting in a total of 7·9 + 7·7 + 7·5 = 147 spin orbital states).

The extended calculations in the d^8+f^8 active space are prohibitive at full CASSCF level, the orbital iterations being performed in the ORMAS (Occupation Restricted Multiple Active Spaces)[34] partition technique, defining two subspaces, one for d^8(Ni) and another for f^8(Tb). Inside each subspace, full CASSCF excitations are performed, allowing only single and double excitations between the two subspaces. The noniterative SO calculations using the ORMAS optimized orbitals were performed at full CAS (complete active space) excitations over the full d^8+f^8 set. Since the account of anisotropy on Tb(III) implies considering 7 states from the ^7F term and the Ni(II) part imposes 10 states resulting from the ^3F+^3P atomic terms (or the $^3A_2$, $^3T_2$, $^3T_1$(F), $^3T_1$(P) in the octahedral reference), the product space implies 70 orbital states for each spin multiplicity. As a whole, the SO implies 210 orbital states for the series of S = 4, 3, 2 spin quantum numbers, which leads to 1470 (i.e., 70·9 + 70·7 + 70·5) spin−orbital states. The complexity of full calculation is suggested in the panel (a) of Figure 9. The Figure 9.a.2 corresponds to the Ni(II) site computed alone, on the $(H_2O)_2NiL$ complex, observing the series of 10 states resulting from actual split of the $^3A_2$, $^3T_2$, $^3T_1$(F), $^3T_1$(P) octahedral parentage. The octahedral idealization represented in Figure 9.a.1 is conventionally obtained taking the average of the three T-type orbital sequences from the Figure 9.a2. The Figure 9.a.3. shows the large number states in the spectrum coming from the complete excitations over the d^8+f^8 active space. The Figure 9.b.3 is a zoom in on the lowest states from the Figure 9.a.3.

With the extended calculation suggested in Figure 9.a.3, the lowest sequence assignable to anisotropic exchange remains also a series of six levels (Figure 9.b.3). The exact degeneracy observed in the above calculations with smaller active space is replaced with a grouping in quasi-degenerate pairs (with spacing of about 0.3 cm^{-1}). In spite of different quantitative details, the schemes represented in Figure 9.b.2 and Figure 9.b.3 are

dx.doi.org/10.1021/ic3001784 | Inorg. Chem. 2012, 51, 11279−11293

qualitatively similar. An interesting fact is that the series of doublets are almost equally spaced.

This splitting scheme suggests an Ising-like phenomenology. In the given situation, the $S_z^{(A)}$ $S_z^{(B)}$ product used in standard Ising expression can be adapted with a J_z projection for the f center, instead of a S_z one, while keeping a S_z factor for the d site, writing $-2j_{df}$ $S_z(d)J_z(f)$. The multiplicity six of the lowest series from CASSCF-SO calculations is given by the product of the effective doublet on lanthanide (as shown in Figure 9.b.1) with the spin triplet on Ni(II). The above considerations dedicated to the local anisotropy of Tb(III) suggested that the lowest doublet can be assigned to the $J_z = \pm 6$ components.

Taking the $J_z = \pm 6$ projections from Tb(III) and $S_z = \pm 1,0$ for the Ni(II) site, the doubly degenerate levels from Figure 9.b.2 or 9.b.3 correspond to the following $S_z(d)J_z(f)$ sequence: {(+1)·(+6), (−1)·(−6)}, {(0)·(+6), (0)·(−6)}, {(−1)·(+6), (+1)·(−6)} with the 0, -12 j_{df}, -24 j_{df} relative energies, respectively. The gaps from Figure 9.b.2 and 9.b.3 sections are fitted with a $j_{df} = 0.31$ cm^{-1} and $j_{df} = 0.57$ cm^{-1}, respectively. The magnetic moments carried by these states correspond to $g_S S_z + g_J J_z$ sums, which with the ideal $g_S = 2$ and $g_J = 3/2$ parameters are ± 11 μ_B, ± 9 μ_B, and ± 7 μ_B, respectively. Thus, in the Ising-like conjuncture, the ferromagnetic pattern in the $\chi_M T$ vs T curve results in a progressive thermal population of states carrying smaller magnetic moment than the ground state. To keep the Ising picture, which seems well certified by advanced calculations, it is not strictly necessary to work with perfect J_z projections, effective or conventional values being sufficient. As shown previously, the state-specific magnetization functions provide effective $g_J J_z$ amounts. Conventional J_z values can be considered, altogether with adjustment factors absorbed into effective g_J. The j_{df} coupling constant can undergo similar rescaling absorbing the factor interconverting effective and conventional J_z numbers. Thus, from such a perspective, the lanthanide can be even considered simplistically by a $s_z = \pm 1/2$ pseudospin,[35] accounting for the doublet local ground state, and a literally Ising formula, $-2j'$ $S_z(d)s_z(f)$, where the factor related with the previous formulation is absorbed in the coupling constant: $j' \equiv 2j_{df}|J_z|$.

The next levels of the full spectrum for the $J = 6$ multiplet keep the grouping in series of three quasi degenerate doublets with the barycenter in each $\pm J_z$ level assigned to the quasi-degenerate doublet from the LF-SO sequence of the lanthanide ion, except a series of three nondegenerate elements assignable to the $J_z = 0$ component.

The revealed scheme of lowest levels enables an explanation for the SMM behavior in the d-f dinuclears. Thus, in the context of Ising-like double degeneracy and ferromagnetic-like ordering, the ground state doublet possesses a maximal moment $\mu_{max} = |g_S S| + |g_J J_z|$, while the higher doublet carries a minimal amount of magnetism $\mu_{min} = \mathrm{abs}(|g_S S| - |g_J J_z|)$. As discussed previously, the $\pm J_z$ components are the same throughout the series, while S_z runs from $-S$ to S, according to the spin on the d site. We can adapt now an explanation similar to the customary heuristic scheme for d complexes, where the relaxation between $+S_z^{max}$ and $-S_z^{max}$ states implies an adiabatic route over a barrier established by the total ZFS gap (implicitly determined by the position of the level with minimal projection S_z^{min}, in a $D < 0$ conjuncture). In turn, here we have the case of a hindered switch between the state with opposite $+\mu_{max}$ and $-\mu_{max}$ magnetizations, the barrier being established by the height of the couple with μ_{min} feature. This perspective is similar to those previously advanced for another dinuclear d-f SMM.[8] The fact that the total gap from the revealed Ising-like scheme is in the same range, 10−15 cm^{-1}, with the U_{eff} relaxation barriers (see section 3.2) can be considered as a support for the presented mechanism. Thus, in d-f systems an Ising-like scheme, tuned by double degenerate ground states on the lanthanide site, seems to be the engine of SMM behavior, when the j_{df} parameter is positive, resulting from the projection of ferromagnetic coupling. However, the smaller implication of the f shell in the chemical bonding makes the adiabatic action coordinate of magnetization relaxation more sensitive to perturbations due to tunnelling splitting. The application of a slight outer field realizes a compromise between keeping the quasidegenerate scheme and decoupling the tunnelling splitting effects which are maximal at degenerate schemes. The actual insight, realized with the help of ab initio results, brings new ideas for the real understanding of the phenomenology in d-f complexes and lanthanide magnetochemistry, and becomes challenging for further advances in this sense. Thus, in the above correlation of the total gap in the lowest term sequence with the U_{eff} barrier, the mechanism of actual hindrance is not specified. In fact, the same lack of detailed understanding persists also in the case of d-complexes, since the celebrated double well potential energy curve drawn over the ZFS spectrum remains merely allusive, the actual reaction coordinate related to this profile being yet not well understood.[36] In case of d-f systems, we tentatively guess that the dipolar effects can play a role in the kinetic part of the SMM effects, but such aspects remain the object of further thorough efforts.

3.6. DFT Calculation the d-f Exchange Coupling in Ni−Gd Complex. As pointed in introduction, the DFT calculations are not well suited for description of lanthanides, but recent advances[12,13] showed a certain possibility to find reasonable solutions in the frame of so-called unrestricted methods, that is, working with different orbital sets for the α and β electrons. The Broken Symmetry (BS) calculations represent a methodology to obtain information about the exchange coupling constant.[37,38] For an A-B dinuclear, the BS treatment implies a couple of unrestricted calculations with different spin projections: $S_z = S_A - S_B$ and $S_z = |S_A - S_B|$. For the Ni−Gd complex one calculation is at the High Spin (HS) multiplicity, $S_z = 9/2$, and another one, for the proper BS state, with $S_z = 5/2$. The HS is the equivalent of the spin decet state, having single-determinant nature, but the BS does not correspond to the sextet of the spin coupling scheme, having in fact no physical reality, being only a helpful hypothetical object. In unrestricted DFT, the S^2 cannot be retrieved as quantum number, $S(S+1)$, being replaced in by its expectation values, $\langle S^2 \rangle$.[39] Note that in BS it is not allowed to conceive intermediate spin multiplicities and states, such as the octet, in this case. Picking the converged energies, E, and the $\langle S^2 \rangle$ quantities from the print-out of the calculations on the HS and BS states, the exchange coupling constant is obtained via the Yamaguchi−Onishi[40] formula:

$$J = \frac{E_{BS} - E_{HS}}{\langle S^2 \rangle_{HS} - \langle S^2 \rangle_{BS}}. \quad (1)$$

The exchange parameter estimated with the B3LYP functional, $J_{NiGd} = +1.26$ cm^{-1}, is in excellent agreement to the experimental one ($J_{NiGd}^{exp} = 1.56$ cm^{-1}).[1] The relevant amounts picked-up from the calculation outputs are illustrated in Table 4. The Mulliken spin populations prove the BS quality

Table 4. Details of the BS-DFT Calculations on the Ni−Gd System with the B3LYP Functional

state	energy (atomic units)	$\langle S^2 \rangle$	Mulliken spin populations	
			Gd	Ni
HS {Gd(7α),Ni(2α)}	−3837.957495	24.765	7.037	1.744
BS: {Gd(7α),Ni(2β)}	−3837.957414	10.765	7.032	−1.743

of the computational experiment, retrieving values close to the {Gd(7α),Ni(2α)} scheme for HS case and {Gd(7α),Ni(2β)} for the BS one. This situation is also well illustrated in Figure 10 plot of the spin density. Note that the achievement of BS quality is nontrivial, since the controls guiding to this result are limited and in many circumstances, instead of obtaining spatially separated α and β orbitals, undesired doubly occupied MOs may result at the end of iterations. One observes that the density maps are similar in absolute contour, but that the BS has the spin reverted around the Ni atom. A part of the spin density in the d-type coordination sphere is delocalized over the surrounding atoms. The density on the f center is almost perfectly spherical, because of the total symmetrical quasi-symmetry of the half-filled shell.

An interesting computation experiment is drawing the density difference of total densities of HS and BS cases (see Figure 11). The total density cumulates the spins with both α and β sources, the maps of HS and BS being similar, because the BS results merely by a spin flip, without affecting much the total electron distribution. The absolute density variation HS vs BS is very small, the absolute integrated difference being integrated to 0.0028 electrons. Even with small absolute magnitude, the distribution of the sign in the difference maps is illustrative for the bonding scheme in this complex. The positive areas (integrated to +0.0014) show shapes resembling the contours (without phase sign) of p-d hybrids at Ni and Gd centers and inward oriented s-p hybrids at phenoxo bridges. The most visible negative areas (integrated to −0.0014) look like *p*-type AOs tangential to the perimeter of diamond-shaped bis-phenoxo bridge. Under the caution of conclusions extrapolated from very weak effects, one may say that the nontrivial information from this map is that the bonding implies in-plane orbital effects related with σ type metal ligand overlap, while no π type differential delocalization seems induced along with the spin flip numerical experiments. We can also speculate from Figure 11 as an illustration that the bonding of lanthanide is realized with the help of outer 5d-type AOs.

3.7. DFT Estimation of the Ligand Field Splitting of the f Shell in the Ni−Tb Complex. The DFT becomes more problematic in describing d-f systems other than those with f^7 configuration. This is because its grounding principles are not defined for degenerate states.[11] However, in asymmetric environments the degeneracy is lifted and even small, the Ligand Field on the f shell enables a certain applicability of DFT in the lanthanide complexes. To the best of our knowledge there are no molecular DFT calculations for other systems than the few reports dedicated to gadolinium complexes.[12,13]

Taking the challenge of using the DFT for calculation of d-f system we propose in the following a new methodological breakthrough, attempting a series of separate DFT calculations handling different orbital configurations of the lanthanide site. The Ni−Tb complex is a convenient case study for the reasons discussed in the section 3.3. Namely, the Tb(III) ion has a ^7F orbital ground state whose orbital components can be described as running the β electron of the f^8 configuration along the f-type orbitals. We exploited this feature attempting to permute the position of β excess electron in unrestricted DFT calculations using corresponding orbital controls in the starting input file. For each situation from the seven configurations mimicking the run along the *F* term components, we performed a HS and a BS calculation (the BS switching only the spins on Ni-type MOs). The fact that we end up with different orbital configurations (e.g., instead of a single preferred configuration) as function of the starting impetus

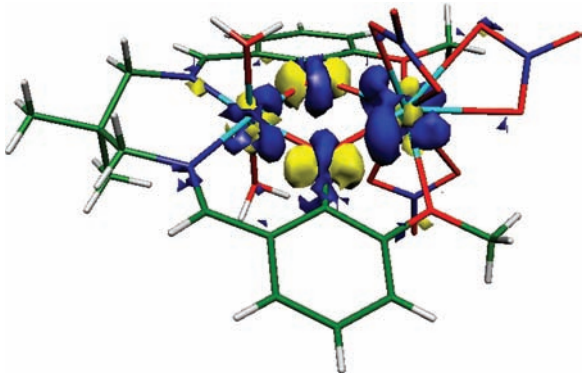

Figure 11. Density difference maps: The HS minus BS total densities from DFT calculations on the Ni−Gd system. The effect, which is extremely weak, is conventionally magnified by drawing contours at very low isosurface values, 0.00001e/Å^3. The positive blue surfaces highlight the zones with slightly higher density in HS system, while the yellow surfaces correspond, on the contrary, to negative difference areas (depletion).

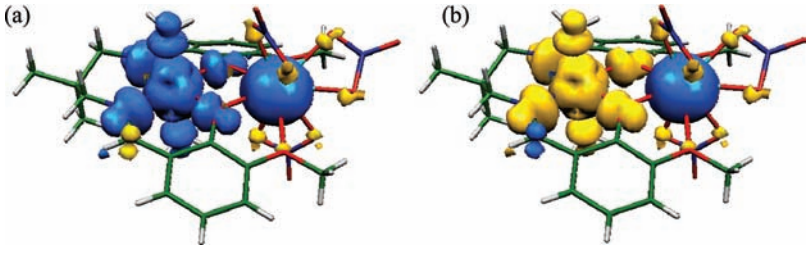

Figure 10. Spin density maps for the DFT calculations on the Ni−Gd system: (a) the HS state, (b) the BS state. The equi-surface is drawn at 0.001e/Å^3, the α zones being depicted in blue, and β ones in yellow. One notes a visible spin delocalization on the donors around Ni(II), with the same sign as the main center (α in HS case, β in BS one) and a very slight spin polarization around Gd(III) site (small β densities around the spherical α surface).

dx.doi.org/10.1021/ic3001784 | *Inorg. Chem.* 2012, 51, 11279−11293

imposed by corresponding orbital permutations is a nontrivial favorable fact.

The relative energies of these various configurations, either in HS or in BS series, are a rough measure of LF splitting of the f shell. The gap between HS and BS at a given configuration yields the exchange coupling constant for that particular situation (using eq 1 as previously explained). Practically, all the HS wave functions have $\langle S^2\rangle_{HS} \approx 20.013$ values and all the BS ones the $\langle S^2\rangle_{BS} \approx 8.014$.

The LF total and individual gaps are probably overestimated (we compare with CASSCF results in 3.3 section), because, in the unrestricted frame, the position of the β electron in the f-type orbitals is not fully equivalent to the position of the doubly occupied f orbital in the LF scheme and therefore the initial reasons in this respect are not fully valid. However, the achievement of separate DFT calculations assignable to LF configurations is an interesting result (particularly considering that DFT is not fully systematically controllable for such goals and that the outcome of a LF-alike series is a fortunate one).

As discussed previously in CASSCF calculations (see Table 3), one may assign a J coupling constant for each configuration. Table 5 shows values ranging between 1 and 1.5 cm^{-1} (except a probable computation failure on line 4), that is, comparable with those obtained previously for the Ni−Gd system. The fact that all the configurations are ferromagnetic-like and quite comparable in magnitude, is a nontrivial finding for such calculations.

Table 5. Results from the Series of Seven DFT Calculations on Ni−Tb Complex (HS and BS Types) Mimicking the LF Split Components Related to the ^7F Term of the Tb(III) Ion[a]

orbital configuration	ΔE_{LF}(HS) (cm^{-1})	J (BS) (cm^{-1})
1	0.0	1.48
2	71.1	0.97
3	359.4	1.19
4	453.3	15.63*
5	1308.7	0.95
6	1620.5	1.42
7	1964.0	1.25

[a]The fourth line is erroneous in the J parameter because of uncontrolled orbital contamination.

An interesting analysis of this series of calculation is done taking the density difference maps (Figure 12) with respect of the total density obtained for the Ni−Gd complex. It is confined to the HS series, taking the Ni−Tb minus Ni−Gd density, for each configuration related to the LF scheme. The conventional procedure is able to map the density due to the supplemental electron, when the f^8 and f^7 configurations are compared. The fact that the resulting molecular density differences are confined nearby the f site do certify that the actual calculations are mimicking qualitatively a LF scheme.

The cuboidal or hexagonal shapes of main density difference contours are similar to the eight- and six- lobe aspect of the standard f AOs (except the phase-sign which is not contained in the full density maps). However, the capability of DFT to account for the LF splitting is limited, as the values from Table 5 show a rather large overestimation of the gaps. Probably for the same reasons it is not easy to establish a clear connection between the canonical orbitals from CASSCF calculations (Figure 5), presented as representative for the LF scheme and the contours from the density difference maps (Figure 12).

4. CONCLUSION

This work presents a series of Ni-Ln complexes (Ln = Tb, Dy, Er, Yb) realized with a compartmental ligand belonging to a class that afforded several prototypical case studies for d-f binuclears.[1,3,5] Although there are no chiral centers in these Ni-Ln complexes, they crystallize in a non centrosymmetric space group $P2_1$. Such a chiral crystallization gives only one enantiomorphic crystal in a 100% yield, contrary to a spontaneous resolution that would give two enantiomers. Another interesting result comes from the observation of ferromagnetic interactions all along the series, from Ni−Gd to Ni−Yb compounds. If such a behavior was previously expected,[27] it has to be noted that it is the first time that it is observed. As a main consequence, out of phase susceptibility

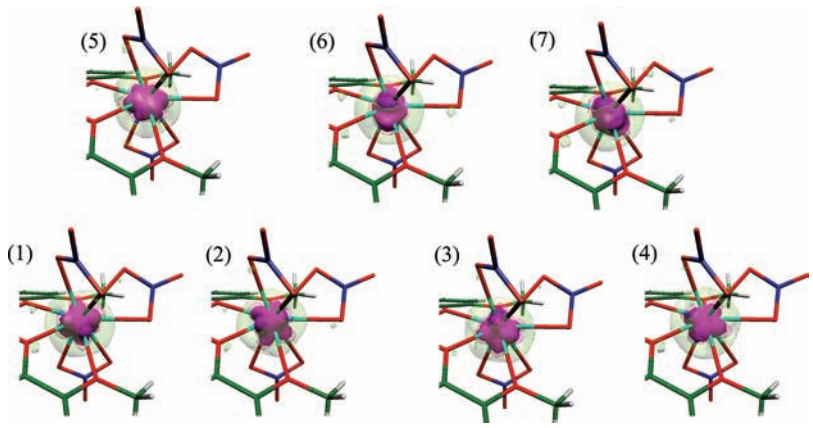

Figure 12. Density difference maps conventionally taken by subtracting the total density of the HS Ni−Gd complex from those corresponding to the seven HS configurations of the Ni−Tb system. The label inside each frame corresponds to the entries 1−7 in Table 5. The numerical experiment is illustrative for the placement of the supplementary f-type density when comparing the f^8 and f^7 configurations. Note that the contours show the octa-lobe or hexa-lobe shapes known for the f orbitals (except the sign of the wave function that cannot be retrieved in a density map). The solid violet surfaces are drawn at 0.01e/Å^{3}values. Another surface at 0.001e/Å^3 is drawn transparently with violet for positive contours (barely visible in the immediate proximity of solid violet shapes) and gray-greenish for negative low density contours visible as a halo (corona). The negative low density contour suggests the slight density polarization around the f site. At this value no contour nearby the d site or the remainder of the ligand is detectable, certifying that the changes along the lanthanide series are due to the f shell.

dx.doi.org/10.1021/ic3001784 | Inorg. Chem. 2012, 51, 11279−11293

signals are found in the Ni−Tb, Ni−Dy, Ni−Er, and Ni−Yb complexes, which is common for the Ni−Tb and Ni−Dy complexes but quite original for the Ni−Er and more particularly for the Ni−Yb entities. The breakthrough presented here consists in an unprecedented deep analysis of rich data, realized with help of various state-of the art and innovative computational methodologies. The ab initio calculations on lanthanide systems cannot be performed following standard routes, our strategies of initiating the procedures with orbitals merged from fragments (with f ions as distinct components) being particularly useful. The multiconfiguration (CASSCF) methods allowed the estimation of d-f exchange effects (in isotropic limit), as well as the realistic Ligand Field account on the f shell. The methods allow even at moderate costs of ingredients (e.g., at medium size basis sets and active spaces limited to the considered d^m-f^n orbital configuration) the calculation of good semiquantitative results that account well for the given phenomenology and underlying mechanisms. The ab initio account of Ligand Field splitting in the f shell allowed us to circumvent in a convenient way the complexities and uncertainties related to the standard phenomenological approach in traditional Ligand Field.[32] For each Ligand Field state one may assign an exchange coupling, the calculations revealing quasi-equal values for the levels resulted from the splitting of the ground orbital multiplet. The calculations obtain the overall ferromagnetic coupling observed experimentally. The magnetic anisotropy is reached adding the spin−orbit (SO) terms, non-iteratively, subsequently to the CASSCF iterative procedures. A particular achievement is the drawing of hereby called state-specific magnetization functions that correspond to the first derivatives of the energy of selected levels from CASSCF-SO Hamiltonian with respect of magnetic field. The polar representation of these functions allows a suggestive picturesque description of the magnetic anisotropy issues on ground and excited states for the considered lanthanide systems. The asymmetric shapes of the magnetization polar diagram for a given state allows the identification of its specific easy magnetization axis. From the extension of corresponding lobes of state specific magnetization diagrams one may infer effective J_z projection quantum numbers. The implication of exchange effects with the LF and SO terms leads to an anisotropic exchange that is found to reproduce an Ising like phenomenology. Such findings are nontrivial and represent significant advances in the understanding of molecular magnetism of d-f complexes. The same methodological advances (CASSCF-SO Hamiltonian of lanthanide sites with incorporated field dependence) afforded the ab initio simulation of $\chi_M T$ vs T curves (for lanthanide site only) that reproduce the background assignable to the lanthanide in the d-f dimers.

Another line of methodological advances was realized collaterally attempting a DFT description of exchange coupling effects (by Broken Symmetry calculations) and a particular mimicking of Ligand Field scheme (by handling orbital permutation facilities of the used code). The DFT seems to account in an excellent manner for the isotropic exchange part, while it is rather deficient in the LF simulation, yielding a rather large overestimation of the energy gaps related to the f shell splitting. The DFT does not have the completeness and leverage power demanded for the complete account of all the effects related to the d-f magnetochemistry, but the possibility of using such frame for particular situations is an interesting prospect.

■ ASSOCIATED CONTENT

Supporting Information

Experimental magnetic data (Figures S1−S3), computation details (Figures S4−S7 and Tables S1−S4), X-ray crystallographic files in CIF format for (**4**) and (**5**). This material is available free of charge via the Internet at http://pubs.acs.org.

■ AUTHOR INFORMATION

Corresponding Author

*E-mail: marilena.cimpoesu@g.unibuc.ro (M.F.), jean-pierre.costes@lcc-toulouse.fr (J.-P.C.).

Notes

The authors declare no competing financial interest.

■ ACKNOWLEDGMENTS

This work was supported by the European Union sixth framework program NMP3-CT-2005-515767 entitled "MAGMANet: Molecular Approach to Nanomagnets and Multifunctional Materials". M.F. acknowledges funds from the research Grants CNCS-UEFISCDI PCE-467/2009 and PCCE 9/2010, Romania. The authors are grateful to Dr. A. Mari for technical assistance.

■ REFERENCES

(1) Costes, J. P.; Dahan, F.; Dupuis, A.; Laurent, J. P. *Inorg. Chem.* **1997**, *36*, 4284−4286.
(2) Matsuura, T.; Koshima, H. *J. Photochem Photobiol. C: Photochem. Rev.* **2005**, *6*, 7−24.
(3) Costes, J. P.; Dahan, F.; Wernsdorfer, W. *Inorg. Chem.* **2006**, *45*, 5−7.
(4) (a) Mishra, A.; Wernsdorfer, W.; Abboud, K. A.; Christou, G. *J. Am. Chem. Soc.* **2004**, *126*, 15648−15649. (b) Ishikawa, N.; Sugita, M.; Wernsdorfer, W. *J. Am. Chem. Soc.* **2005**, *127*, 3650−3651.
(5) Paulovic, J.; Cimpoesu, F.; Ferbinteanu, M.; Hirao, K. *J. Am. Chem. Soc.* **2004**, *126*, 3321−3331.
(6) (a) Costes, J. P.; Dahan, F.; Dupuis, A.; Laurent, J. P. *Inorg. Chem.* **2000**, *39*, 169−173. (b) Laurent, J. P.; Dahan, F.; Dupuis, A. *Inorg. Chem.* **2000**, *39*, 5994−6000.
(7) (a) Benelli, C.; Gatteschi, D. *Chem. Rev.* **2002**, *102*, 2369−2387, and references therein. (b) Kahn, O. *Acc. Chem. Res.* **2000**, *33*, 647−657. (c) Sakamoto, M.; Manseki, K.; Okawa, H. *Coord. Chem. Rev.* **2001**, *379*, 219−221 , and references therein. (d) Andruh, M.; Costes, J. P.; Diaz, C.; Gao, S. *Inorg. Chem.* **2009**, *48*, 3342−3359.
(8) Ferbinteanu, M.; Kajiwara, T.; Choi, K. −Y.; Nojiri, H.; Nakamoto, A.; Kojima, N.; Cimpoesu, F.; Fujimura, Y.; Takaishi, S.; Yamashita, M. *J. Am. Chem. Soc.* **2006**, *128*, 9008−9009.
(9) (a) Schmidt, M. W.; Gordon, M. S. *Annu. Rev. Phys. Chem.* **1998**, *49*, 233−266. (b) Roos, B. O. *Lect. Notes Quantum Chem.* **1994**, *58*, 177−254.
(10) Hirao, K., Ed.; *Recent Advances in Multi-Multireference Methods*; World Scientific: Singapore, 1999.
(11) Koch, W.; Holthausen, M. C. *A Chemist's Guide to Density Functional Theory*; Wiley-VCH: Berlin, Germany, 2001.
(12) Rajaraman, G.; Totti, F.; Bencini, A.; Caneschi, A.; Sessoli, R.; Gatteschi, D. *Dalton Trans.* **2009**, 3153−3161.
(13) Singh, S. K.; Tibrewal, N. K.; Rajaraman, G. *Dalton Trans.* **2011**, *40*, 10897−10906.
(14) Costes, J. P.; Donnadieu, B.; Gheorghe, R.; Novitchi, G.; Tuchagues, J. P.; Vendier, L. *Eur. J. Inorg. Chem.* **2008**, 5235−5244.
(15) Pascal, P. *Ann. Chim. Phys* **1910**, *19*, 5−70.
(16) *CrysAlis RED*, version 1.170.32; Oxford Diffraction Ltd.: Abingdon, U.K., 2003.
(17) *SHELX97 [Includes SHELXS97, SHELXL97, CIFTAB] - Programs for Crystal Structure Analysis* (Release 97-2); Sheldrick, G. M. Institut für Anorganische Chemie der Universität Göttingen: Göttingen, Germany, 1998.

(18) Farrugia, L. *J. Appl. Crystallogr.* **1999**, *32*, 837−838.
(19) *International tables for X-Ray crystallography*; Kynoch press: Birmingham, England, 1974; Vol *IV*.
(20) Zsolnai, L.; Pritzkow, H.; Huttner, G. *ZORTEP, Ortep for PC, Program for Molecular Graphics*; University of Heidelberg: Heidelberg, Germany, 1996.
(21) Schmidt, M. W.; Baldridge, K. K.; Boatz, J. A.; Elbert, S. T.; Gordon, M. S.; Jensen, J. H.; Koseki, S.; Matsunaga, N.; Nguyen, K. A.; Su, S. J.; Windus, T. L.; Dupuis, M.; Montgomery, J. A. *J. Comput. Chem.* **1993**, *14*, 1347−1363.
(22) (a) Stevens, W. J.; Basch, H.; Krauss, M. *J. Chem. Phys.* **1984**, *81*, 6026−6033. (b) Stevens, W. J.; Krauss, M.; Basch, H.; Jasien, P. G. *Can. J. Chem.* **1992**, *70*, 612−630. (c) Cundari, T. R.; Stevens, W. J. *J. Chem. Phys.* **1993**, *98*, 5555−5565.
(23) (a) Alvarez, S.; Avnir, D.; Llunell, M.; Pinsky, M. *New J. Chem.* **2002**, *26*, 996−1009. (b) Ruiz Martinez, A.; Alvarez, S. *Chem.—Eur. J.* **2009**, *15*, 7470−7480.
(24) The powder XRD patterns were collected on a XPert Pro (θ-θ mode) Panalytical diffractometer with λ (Cu $K_{\alpha1}$, $K_{\alpha2}$) = 1.54059−1.54439 Å.
(25) Maurice, R.; Vendier, L.; Costes, J. P. *Inorg. Chem.* **2011**, *50*, 11075−11081.
(26) Costes, J. P.; Dahan, F.; Dupuis, A.; Laurent, J. P. *Chem.—Eur. J.* **1998**, *4*, 1616−1620.
(27) Andruh, M.; Ramade, I.; Codjovi, E.; Guillou, O.; Kahn, O.; Trombe, J. C. *J. Am. Chem. Soc.* **1993**, *115*, 1822−1830.
(28) Sutter, J. P.; Dhers, S.; Costes, J. P.; Duhayon, C. *C. R. Chim.* **2008**, *11*, 1200−1206.
(29) (a) Chandrasekhar, V.; Murugesa Pandian, B.; Boomishankar, R.; Steiner, A.; Vittal, J. J.; Houri, A.; Clérac, R. *Inorg. Chem.* **2008**, *47*, 4919−4929. (b) Pasatoiu, T. D.; Sutter, J. P.; Madalan, A. M.; Chiboub Fellah, F. Z.; Duhayon, C.; Andruh, M. *Inorg. Chem.* **2011**, *50*, 5890−5898. (c) Chandra Mondal, K.; Kostakis, G. E.; Lan, Y.; Wernsdorfer, W.; Anson, C. E.; Powell, A. K. *Inorg. Chem.* **2011**, *50*, 11604−11611.
(30) Pierloot, K. In *Computational Organometallic Chemistry*; Cundari, T. R., Ed.; Marcel Dekker Inc.: New York, 2001; pp 123−158.
(31) (a) Nakano, H. *J. Chem .Phys.* **1993**, *99*, 7983−7992. (b) Hirao, K. *Chem. Phys. Lett.* **1993**, *201*, 59−66. (c) Nakano, H.; Nakayama, K.; Hirao, K.; Dupuis, M. *J. Chem. Phys.* **1997**, *106*, 4912−4917. (d) Ivanic, J.; Ruedenberg, K. *Theor. Chem. Acc.* **2001**, *106*, 339−351.
(32) (a) Newman, D. J.; Ng, B. K. C. *Crystal Field Handbook*, Cambridge University Press: Cambridge, U.K., 2000; (b) Klokishner, S. I.; Ostrovsky, S. M.; Reu, O. S.; Palii, A. V.; Tregenna-Piggott, P. L. W.; Brock-Nannestad, T.; Bendix, J.; Mutka, H. *J. Phys. Chem. C* **2009**, *113*, 8573−8582.
(33) Ferbinteanu, M.; Cimpoesu, F.; Gîrţu, M. A.; Enachescu, C.; Tanase, S. *Inorg. Chem.* **2012**, *51*, 40−50.
(34) Ivanic, J. *J. Chem. Phys.* **2003**, *119*, 9364−9376, 9377−9385.
(35) (a) Prins, F.; Pasca, E.; de Jongh, L. J.; Kooijman, H.; Spek, A. L.; Tanase, S. *Angew. Chem., Int. Ed.* **2007**, *46*, 6081−6084. (b) Tanase, S.; de Jongh, L. J.; Prins, F.; Evangelisti, M. *Chem. Phys. Chem.* **2008**, *9*, 1975−1978.
(36) Gatteschi, D.; Sessoli, R. *Angew. Chem., Int. Ed.* **2003**, *42*, 268−297.
(37) (a) Daul, C. A.; Ciofini, I.; Bencini, A. In *Reviews of Modern Quantum Chemistry*, part II; Sen, K. D., Ed.; World Scientific: Singapore, 2002; 1247. (b) Noodleman, L.; Peng, C. Y.; Case, D. A.; Mouesca, J. M. *Coord. Chem. Rev.* **1995**, *144*, 199−244.
(38) Ruiz, E. *Struct. Bonding (Berlin)* **2004**, *113*, 71−102.
(39) Bulo, R. E.; Ehlers, A. W.; Grimme, S.; Lammertsma, K. *J. Am. Chem. Soc.* **2002**, *124*, 13903−13910.
(40) (a) Onishi, T.; Takano, Y.; Kitagawa, Y.; Kawakami, T.; Yoshioka, Y.; Yamaguchi, K. *Polyhedron* **2001**, *20*, 1177. (b) Nagao, H.; Nishino, M.; Shigeta, Y.; Soda, T.; Kitagawa, Y.; Onishi, T.; Yoshioka, Y.; Yamaguchi, K. *Coord. Chem. Rev.* **2000**, *198*, 265−295.